RSC Advances

PAPER

View Article Online
View Journal | View Issue

Cite this: *RSC Adv.*, 2020, **10**, 2767

Synthesis, characterization, and comparison of antibacterial effects and elucidating the mechanism of ZnO, CuO and CuZnO nanoparticles supported on mesoporous silica SBA-3†

Songfa Qiu, Hongjun Zhou,* Zhichuan Shen, Li Hao, Huayao Chen and Xinhua Zhou*

Received 24th November 2019
Accepted 8th January 2020

DOI: 10.1039/c9ra09829a

rsc.li/rsc-advances

Silanized iminodiacetic acid (GLYMO–IDA) modified mesoporous silica (G-SBA) was prepared following a co-condensation method. G-SBA/Cu^{2+}, G–SBA/Zn^{2+} and G-SBA/Cu^{2+}–Zn^{2+} were obtained through the impregnation method with coordination by GLYMO–IDA. SBA/CuO, SBA/ZnO, and SBA/CuZnO were generated after calcination of G-SBA/Cu^{2+}, G-SBA/Zn^{2+} and G-SBA/Cu^{2+}–Zn^{2+}. After modification, the amount of metal ion was 6 to 70 times higher than that of the blank mesoporous silica. The diameter of nano-copper oxide particles in mesoporous silica was 4.8 nm. The bacteriostatic rates of SBA/CuO at a copper oxide concentration of 250 ppm against *E. coli* and *S. aureus* were 85.87% and 100%, respectively. SBA/CuO and SBA/CuZnO with {111} lattice planes exhibited better antibacterial effects compared to the commercial-grade nano-zinc oxide and nano-copper oxide. When exposed to ultraviolet light, SBA/CuZnO displayed the highest photocatalytic activity and optimal antimicrobial effect. Therefore, SBA/CuZnO can be an alternative to antibiotics because of its non-toxic nature and good antibacterial properties.

1. Introduction

Metal oxide nanoparticles are extensively utilized in catalysts, energy storage materials and antibacterial agents.[1–3] Due to some obvious advantages, such as low cost, nontoxicity, and long-acting antibacterial properties, these metal oxide nanoparticles (NPs) can be applied as a substitute for veterinary antibiotics in animal feed.[4–6] Nowadays, numerous antibiotic substitutes have been developed. Many alternatives, including probiotics, prebiotics and metals have been tested in the poultry industry.[7–9] In recent years, novel alternatives have been developed.[10,11]

Among them, metal oxide NPs are popular due to their high volume ratio and photocatalytic effect, which endow effective antibacterial properties to the metal oxide NPs.[12] ZnO, CuO, Fe_2O_3, and Ag_2O possess good antibacterial properties, and their bacteriostatic mechanism is different. Bactericidal and bacteriostatic mechanisms of ZnO NPs involve the generation of reactive oxygen species (ROS).[13] CuO NPs mainly release metal ions and copper-containing substances, and thus, they inactivate the microbes by promoting oxidative stress reaction, destroying membrane integrity and binding to the proteins.[14] However, the pure ZnO NPs have some drawbacks: they agglomerate during sterilization or antibacterial and inefficient utilization of visible light. Two strategies can be adopted to solve these problems. For improving the utilization of visible light by ZnO NPs,[15,16] the recombination of charge carriers of ZnO could be reduced by combining the photocatalysts with CuO. Furthermore, a synergistic antimicrobial effect could be built between ZnO and CuO, as CuO act as an antibacterial agent itself among bimetal oxide system. The dispersibility of ZnO nanoparticles can be improved by hollow carriers, such as silica-coated structured ZnO nanomaterials.[17]

Mesoporous silica materials are non-toxic, biocompatible, blessed with tunable pore diameter.[18] Co-polycondensation and post grafting are two processes for preparing functionalized mesoporous silica.[19] Shen[20] prepared salicylaldimine modified mesoporous silica through a co-condensation method and loaded it with zinc oxide. The highest load of ZnO NPs on salicylaldimine modified MCM-41 had an atomic concentration of 2.03%. Enshirah Da'na[19] summarizes the application of functionalized mesoporous silica to the adsorption of heavy metals, showing the advantages of mesoporous silica in the modification of organic groups and the adsorption of metal ions. Issa M. El-Nahhal[21] prepared silica coated MgO-NPs composites, functionalization with thiolorgano functional silane precursor. After

Key Laboratory of Agricultural Green Fine Chemicals of Guangdong Higher Education Institution, School of Chemistry and Chemical Engineering, Zhongkai University of Agriculture and Engineering, Guangzhou, People's Republic of China. E-mail: hongjunzhou@163.com; cexinhuazhou@163.com

† Electronic supplementary information (ESI) available. See DOI: 10.1039/c9ra09829a

hydrochloric acid treatment, it can be used for extraction and removal of dyes. Malhotra[22] prepared 5-Na/ZnO loaded SBA-15 and used it as a catalyst for trans-esterifying virgin cottonseed oil; it displayed highly efficient and stable catalysis catalytic by reaching to 74% in 5th cycle after regeneration. However, only a few studies have investigated the bactericidal properties of mesoporous silica supported nano metal oxides. Yue Tian[23] reported that MCM-41 decorated with silver nanoparticles could enhanced the antibacterial ability of sliver nanoparticles. In addition, Ag-MSNs did not affect human body at an effective antibacterial concentration. DarjaMaučec[24] prepared mesoporous silica-supported ZnO and TiO_2 photocatalyst, which could treat dye waste water at a neutral pH. Maryam Rajabzadeh[25] synthesized a hollow mesoporous silica-supported copper oxide catalyst to catalyze the synthesis of 1,2,3-triazole compounds. Anna Donnadio[26] prepared two zinc oxide-loaded mesoporous silica, which exhibited the ability to resist bacteria and fungi.

The photocatalytic efficiency of ZnO was low because of its wide bandwidth. So, its charge could not be effectively separated. This problem can be effectively solved by coupling the semiconductors of different energy levels.[27,28] The combination of double metal oxides can transfer the charge in time and improve the photocatalytic effect of zinc oxide. Abdus Samad[29] prepared a photocatalyst by mixing copper oxide and zinc oxide for catalyzing the oxidation of arsenic. The photocatalytic performance of the mixture was up to four times higher than that of the original zinc oxide.

In this study, we were prepared the SBA-3 decorated with nano metal oxide (SBA/ZnO, SBA/CuO, SBA/CuZnO) in extremely dilute hydrochloric acid solution. The loading, crystalline state and dispersion properties of metal oxide and the particle size, pore parameters and order degree of mesoporous silica were analyzed. We also studied the release of hydrogen peroxide and metal ions for understanding the antibacterial mechanism and evaluated the antibacterial activity. Moreover, the antibacterial properties of SBA/CuZnO were investigated under photocatalytic conditions and compared them to SBA/CuO and SBA/ZnO.

2. Experiments

2.1. Materials

Cetyl trimethyl ammonium bromide (CTAB), glycidyloxypropyltrimethoxysilane (GLYMO), tetraethyl orthosilicate (TEOS), iminodiacetic acid, nano-copper oxide (40 nm) and nano-zinc oxide (40 nm) were all provided by Shanghai Aladdin Biochemical Reagents (Shanghai, China). Hydrochloric acid (wt% = 36–38%), ethanol, sodium hydroxide, potassium bromide, and sodium chloride were provided by Tianjin Damao Chemical Reagents (Tianjin, China). LB nutrient agar and LB broth were obtained from Beijing Solarbio Life Sciences Reagents (Beijing, China).

2.2. Instruments

Fourier Transform Infrared (FTIR) spectroscopy was performed using a Spectrum 100 FTIR (PerkinElmer, USA) in the range of 4000–400 cm^{-1} following the KBr squash technique. Brunauer–Emmett–Teller (BET) adsorption–desorption isotherm was operated on a Quadrasorb SI adsorption equipment (Quantachrome, USA) after degassing for 4 h at 473.15 K. zeta potentials were measured using a Zetasizer Nano ZS (Bruker Corporation, Germany) in water after ultrasound-assisted dispersion. Small-angle X-ray scattering (SAXS) was recorded using a Saxesess mc^2 X-ray diffractometer (Anton Paar, Austria) with copper target, 40 kV, 50 mA and 0.08–5° of test angle range. The crystal morphology of the samples was analyzed by D8 advance X-ray diffraction (XRD) (Bruker, Germany) with copper target and a graphite monochromator at 25 °C, 40 kV, and 30 mA. The scanning speed was 2° min^{-1} (angular range 2θ = 5–90°) in a 0.02 step size. Raman spectra were recorded by a DXR2 Raman microscope (Thermo Fisher Scientific, USA), using the 532 nm excitation line and keeping a constant power of 10 mW. The sample was characterized using a QUANTA250 thermal field emission scanning electron microscope (FEI, USA) after gold coating under vacuum. Transmission electron microscopic (TEM) images and high-resolution transmission electron micrographs (HRTEM) coupled with elected area electron diffraction (SAED) were recorded using a FEI Tecnai TF20 transmission electron microscope (Thermo Fisher Scientific, USA). X-ray photoelectron spectroscopy (XPS) was performed using an ESCALAB 250Xi X-ray spectrometer (Thermo Fisher Scientific, USA) under a vacuum of 2×10^{-7} Pa, Al Kα and $h\nu$ = 1486.6 eV. The content of Zn element was determined using an Agilent 725 inductively coupled plasma optical emission spectrometer (ICP-OES, Agilent, USA). The ultraviolet-visible diffuse reflection (UV-vis DRS) was recorded at room temperature using a U4100 UV-vis spectrophotometer (Hitachi, Japan). A TGA2 thermogravimetric analyzer (TGA, Mettler-Toledo, USA) was analyze over the heating range of 40–800 °C at a heating rate of 10 °C min^{-1} under the nitrogen atmosphere of 50 mL min^{-1}.

2.3. Preparation of GLYMO–IDA

According to a published method,[30] 4.2 g of iminodiacetic acid (IDA) and 2.8 g of NaOH was added in 50 mL ultrapure water, and stirred at 0 °C on an ice water bath. Then, 1.4 mL of silane coupling agent KH560 was dropped, and the stirring was continued. The flask was cooled down on an ice water bath at 0 °C. Then, the reaction mixture was placed on a water bath at 65 °C and stirred at 400 rpm for 6 h. At last, the pH was adjusted to 6.0 with HCl and stored at 4 °C.

2.4. Preparation of SBA-3 and G-SBA

Mesoporous silica particles of SBA-3 were prepared by hydrothermal method. In brief, 42.5 mL of hydrochloric acid was added to 212.5 mL of mechanically stirred at 255 rpm deionized water on an oil bath at 63 °C. Then added 3.4 g of CTAB to the solution with continuous stirring. After the solution became stable, added 14.1 g of TEOS to the solution dropwise at 1 drop per second; stirred the mixture for 6 h, and crystallized on an oil bath at 33 °C for one day. The mixture was then filtered, washed, and placed at 60 °C overnight. At last, SBA-3 was obtained by calcinating at 550 °C for 6 h.

For G-SBA particles, the above procedure was followed. Then, 4.7 g of GLYMO–IDA was added, and the reaction was stopped after mixing evenly for 20 min. The product crystallized at 33 °C for 24 h, and then filtered, washed, and placed at 60 °C overnight. Finally, the template was removed by extracting in absolute ethanol for 3 days in a Soxhlet extractor to obtain G-SBA.

2.5. Preparation of metal oxide supported by modified mesoporous silica and mesoporous silica-mixed metal oxide

For mesoporous silica nano-zinc oxide particles, added 500 mg of G-SBA to 100 mL of 2 M zinc nitrate solution at 25 °C and stirred for 24 h, and then filtered, washed, and placed at 60 °C overnight. At last, zinc ions were converted to nano zinc oxide by calcinating at 550 °C for 10 h to gain SBA/ZnO. SBA/CuO and SBA/CuZnO were prepared following the same procedure as SBA/ZnO. The procedure is outlined in Fig. 1. The physically mixed samples of mesoporous silica and commercial nano metal oxide (SBA + ZnO, SBA + CuO and SBA + CuZnO) were mixed uniformly, and a mixing ratio was obtained according to the test results of ICP of SBA/ZnO, SBA/CuO, and SBA/CuZnO.

2.6. Determination of viable cell number

The number of viable cells was determined using *Staphylococcus aureus* (*S. aureus* CGMCC) and *Escherichia coli* (*E. coli* CGMCC) as model strains. Typically, 1 mg, 2 mg, 3 mg, 4 mg and 5 mg of SBA-3, SBA/ZnO, SBA/CuO, and SBA/CuZnO powders, respectively were added to Erlenmeyer flasks containing 20 mL of LB agar, previously cooled to 50 °C. Then, 100 μL of each of *S. aureus* (10^5 CFU mL^{-1}) and *E. coli* (10^5 CFU mL^{-1}) were transferred into the plates, 20 mL of LB agar were poured into it, and dried for 30 min, incubated at 37 °C for 24–72 h and recorded optical images finally. In addition, 5 mg of mesoporous silica and commercial grade nano-metal oxide were mixed in proportion to carry out the same test. To determine the antibacterial rate, the following eqn (1) was used for calculation:[31]

$$\eta = \frac{n_0 - n}{n_0} \times 100\% \quad (1)$$

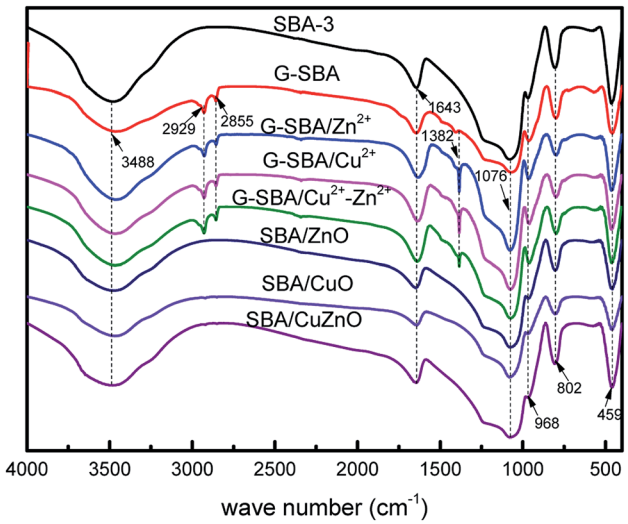

Fig. 2 FTIR spectra of SBA-3, G-SBA, G-SBA/Zn^{2+}, G-SBA/Cu^{2+}, G-SBA/Cu^{2+}–Zn^{2+}, SBA/ZnO, SBA/CuO and SBA/CuZnO.

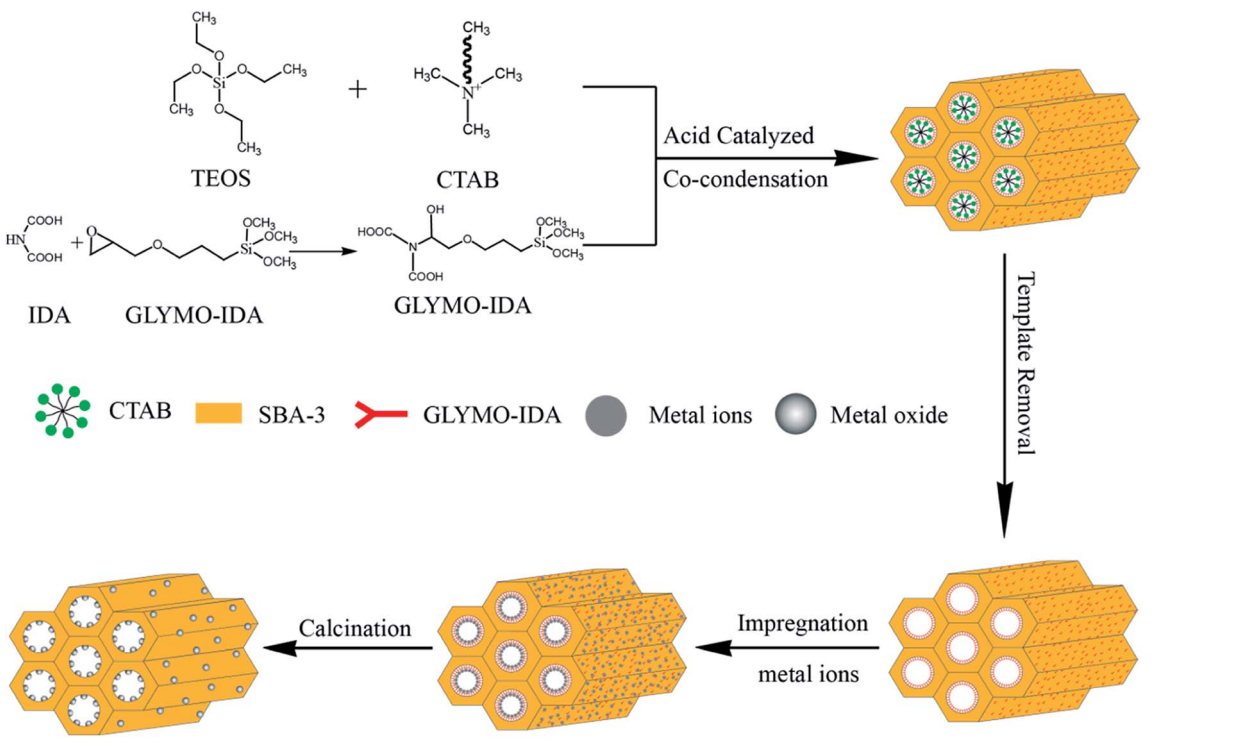

Fig. 1 Sketch map of the synthetic of SBA/ZnO, SBA/CuO, and SBA/CuZnO.

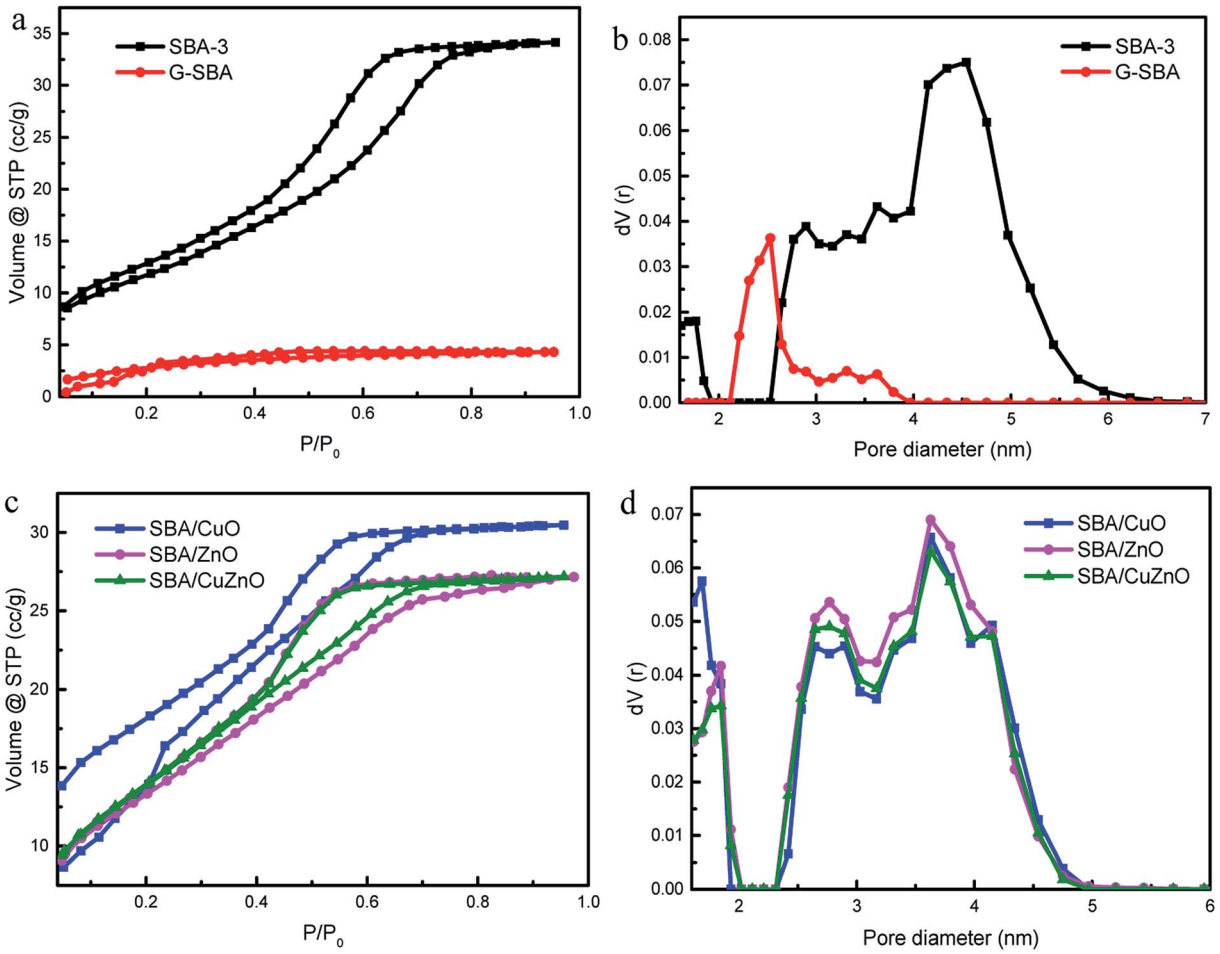

Fig. 3 N_2 adsorption/desorption isotherms (a and c) and pore size distribution (b and d) of SBA-3, G-SBA, SBA/CuO, SBA/ZnO and SBA/CuZnO.

where η is the antibacterial rate, %; n_0 and n are the numbers of viable bacterial cells in the absence and presence of SBA-3 and other materials, respectively, cfu mL^{-1}.

2.7. Determination of H_2O_2

The release of H_2O_2 from SBA/CuO, SBA/ZnO, and SBA/CuZnO suspensions was determined by UV-vis spectrophotometry using KI and starch according to the literature.[32] Briefly, 1 mg mL^{-1} suspension of SBA/CuO, SBA/ZnO and SBA/CuZnO were illuminated under 1100 W UV and stirred at 200 rpm for 2 h after ultrasonication in the dark (the control group was stirred in the dark). The absorbance of the filtrate was detected by scanning from 400 nm to 750 nm through a UV-vis spectrophotometer.

2.8. Minimum inhibitory concentration (MIC) and minimum bactericidal concentration (MBC)

According to the literature,[33] the selected NPs were prepared twelve concentrations, which were 100, 50, 25, 12.5, 6.25, 3.125, 1.563, 0.781, 0.391, 0.195, 0.098 and 0.049 mg mL^{-1} for each of SBA/CuO, SBA/ZnO and SBA/CuZnO NPs. The order of addition was always LB broth, NPs, and then bacteria. Row A and row H were the negative and positive controls. The absorbance was measured by the microplate reader on the OD_{600}. Each isolate was determined in triplicate.

2.9. Determination of metal ions

The suspensions of SBA/CuO, SBA/ZnO and SBA/CuZnO at concentration of 1 mg mL^{-1} were stirred at 200 rpm for 2 h under 1100 W UV after ultrasonication in the dark (the control-group was stirred in the dark). Then, the samples were removed from suspensions by centrifuging (6000 rpm, 5 min). The concentration of Zn^{2+} or Cu^{2+} was measured by ICP-OES.

Table 1 The pore structural parameters of SBA-3, G-SBA, SBA/CuO, SBA/ZnO, and SBA/CuZnO

Materials	Surface area (m^2 g^{-1})	Pore diameter Dv (nm)	Pore volume (m^3 g^{-1})
SBA-3	642	4.5426	0.670
G-SBA	163	2.5308	0.034
SBA/CuO	1060	3.6274	0.472
SBA/ZnO	827	3.6274	0.436
SBA/CuZnO	829	3.6274	0.397

Table 2 Zeta potential of SBA-3, G-SBA, SBA/CuO, SBA/ZnO and SBA/CuZnO

Materials	SBA-3	G-SBA	SBA/CuO	SBA/ZnO	SBA/CuZnO
Zeta potential (mV)	-23.82 ± 0.35	-27.15 ± 0.41	-16.13 ± 0.85	-17.08 ± 1.03	-17.41 ± 0.96

2.10. Photocatalytic antibacterial activity

The photocatalytic antibacterial activity of SBA/CuO, SBA/ZnO, and SBA/CuZnO mesoporous silica composite was evaluated by the inactivation of *S. aureus* after the samples under the ultraviolet light treatment. In short, disperse 3 mg of the samples in 5 mL of deionized water and irradiated under a 1100 W UV lamp for 1 h. After the irradiation, 20 mL of agar was added, and the bacteria were cultured for 24 h by agar dilution method, followed by bacterial count.

3. Results and discussion

3.1. FTIR analysis

In Fig. 2, the FTIR spectra of the different compositions of SBA-3, G-SBA, G-SBA/Zn^{2+}, G-SBA/Cu^{2+}, G-SBA/Cu^{2+}–Zn^{2+}, SBA/ZnO, SBA/CuO, and SBA/CuZnO were compared. For SBA-3, the peaks, appeared at about 3488 and 1643 cm^{-1}, attributed to stretching and bending vibrations of O–H. The peaks of Si–O–Si were observed at 1076, 802 and 459 cm^{-1}. The strong peak at 968 cm^{-1} generated by the stretching vibrations of Si–O–H. Compared to SBA-3, three new bands at 2929, 2855 and 1382 cm^{-1} in the spectra of G-SBA, G-SBA/Zn^{2+}, G-SBA/Cu^{2+} and G-SBA/Cu^{2+}–Zn^{2+} were the C–H stretching and bending vibration of GLYMO–IDA. These spectra confirm that GLYMO–IDA is present in the skeleton of SBA-3. In the spectra of SBA/ZnO, SBA/CuO, SBA/CuZnO, the bands at 2929, 2855 and 1382 cm^{-1} disappeared, because GLYMO–IDA was calcined and decomposed at 550 °C.

3.2. BET analysis

Fig. 3 depicts the N_2 adsorption/desorption isotherms and pore diameters of the pure SBA-3, G-SBA, SBA/CuO, SBA/ZnO, and SBA/CuZnO. Table 1 displays a comparison of the pore structural parameters of five samples. The SBA-3, SBA/CuO, SBA/ZnO, and SBA/CuZnO display type IV isotherms with H_2 hysteresis loops, which characterize the mesopore structure, and according to the IUPAC classification, they indicate ink bottle pores. The information of hysteresis loop shows a narrow pore size distribution.[34] The capillary condensation of nitrogen was caused the sharply increased of isotherms at a relative pressure (P/P_0) of 0.4.[35] Most importantly, the BET surface area, pore volume and pore size of organic molecules co-polycondensed mesoporous silica G-SBA was all declined, which indicated that organic molecules were modified in the tunnel and surface. Fig. 3b and d depict the pore size distributions, obtained by the BJH analyses and pore volumes, obtained by DFT analyses. SBA-3, SBA/CuO, SBA/ZnO, and SBA/CuZnO displayed two kinds of pore size distributions – a small number of micropores and mostly mesoporous structures, while only one mesopore system, with a relatively large smaller pore size, was observed for G-SBA. It was possible that the narrower tunnel structure was formed by adding GLYMO–IDA into the mesoporous silica. In addition, the reduction in the surface area, pore diameter and pore volume of G-SBA (Table 1) suggest that GLYMO–IDA at the inner surface of the mesoporous silica exerted the blocking effect. Furthermore, the BET surface of G-SBA decreased to 163 $m^2\ g^{-1}$, and the average pore diameter decreased to 2.531 nm compared to SBA-3. The surface areas of SBA/CuO, SBA/ZnO and SBA/CuZnO increased but the pore diameter and pore volume decreased. The increase in surface area is due to the calcination and decomposition of the complexed GLYMO–IDA with metal ions and formation of the metal oxide nanoparticles. The pore size and pore volume were smaller than SBA-3 because the metal oxide was present in the mesoporous silica channel.

3.3. Zeta potential analysis

Compared to SBA-3, the zeta potential of G-SBA negatively shifted from -23.82 ± 0.35 to -27.15 ± 0.41 eV due to the negative ions from the carboxyl group of GLYMO–IDA (Table 2). The zeta potentials of SBA/CuO, SBA/ZnO and SBA/CuZnO positively shifted from -23.82 ± 0.35 eV to -16.13 ± 0.85 eV, -17.08 ± 1.03 eV and -17.41 ± 0.96 eV, respectively. This result proved that the nano ZnO, CuO and CuZnO was supported on the mesoporous silica.[36]

3.4. SAXS analysis

Fig. 4 displays the SAXS of SBA-3, G-SBA, SBA/CuO, SBA/ZnO, SBA/CuZnO. In the spectrum of SBA-3, a strong peak appeared

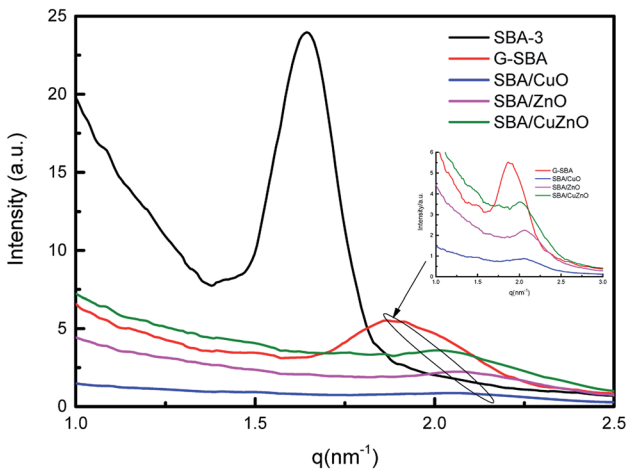

Fig. 4 SAXS profiles measured on reflexion on five representative samples: SBA-3, G-SBA, SBA/CuO, SBA/ZnO, SBA/CuZnO.

at $q = 1.64$ nm^{-1}, attributing to the (100) planes. The d_{100} spacing is 3.83 nm, and a_0 (pore to pore distance) is 4.42 nm. SAXS pattern of G-SBA shows a weak peak at $q = 1.87$ nm^{-1} due to (110) planes. SAXS patterns of SBA/ZnO and SBA/CuO display a weak peak at $q = 2.06$ nm^{-1} attributing to the (200) planes. The (200) planes of SBA/CuZnO has a little move to $q = 2.01$ nm^{-1}. These three planes *i.e.* (100), (110) and (200), are connected with the two-dimensional hexagonal structure (space group *P6mm*).[37] The disappearance of (100) in the curves of G-SBA, SBA/CuO, SBA/ZnO, and SBA/CuZnO was due to the introduction of organic functional groups and metal oxide, which assisted the mesoporous silica to form a non-ideal two-phase system.[38]

3.5. XRD analysis

Fig. 5a shows wide-X-ray diffraction patterns (WXRD) of G-SBA, SBA/CuO, SBA/ZnO, and SBA/CuZnO, where all samples exhibit a wide peak at 2θ values of 23.0° due to the non-crystalline silica.[39–41] Compared to SBA-3, SBA/ZnO diffractogram exhibits no other crystal peaks, which means that they are present in non-crystalline small clusters of ZnO. For SBA/CuO and SBA/CuZnO mesoporous silica compositions, except for the broad diffuse peak of SBA-3, two extra characteristic peaks can be observed at 2θ values of 35.5° and 38.7°, corresponding to the (−111) and (111) reflections, respectively. These two peaks indicate that the CuO generated into the mesoporous silica was the monoclinic phase.[42] However, the diffuse peaks of ZnO in SBA/CuZnO diffraction pattern disappears, because the load of ZnO in SBA/CuZnO is rare (shown in ICP and XPS). Fig. 5b is the SAED pattern of SBA/ZnO. It is shows that ZnO exists in amorphous form in mesoporous silicon.

3.6. Raman spectra analysis

Fig. 6 shows the Raman spectra of SBA-3, SBA/ZnO, SBA/CuO, and SBA/CuZnO. SBA-3 exhibits Raman features at 487, 607, 804 and 972 cm^{-1}. The bands at 487 and 607 cm^{-1} appeared due to the siloxane rings generated by the condensation of surface hydroxyls. The bands at 804 and 972 cm^{-1} appeared

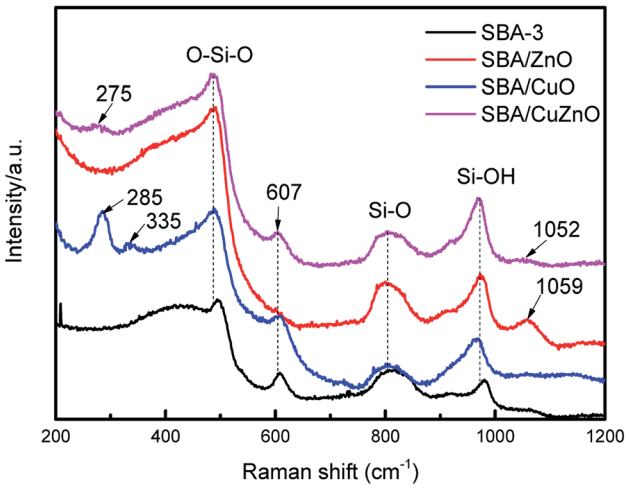

Fig. 6 Raman spectra of the SBA-3, SBA/ZnO, SBA/CuO, and SBA/CuZnO.

owing to the symmetric stretching modes of the siloxane linkages and Si–OH stretching of the surface silanol, respectively.[43] The SBA/CuO displays two new peaks at 285 and 335 cm^{-1}, which is in accordance with the generation of CuO.[44] The band at 1059 cm^{-1} of SBA/ZnO is due to the second-order Raman active modes of ZnO.[45] In SBA/CuZnO, the bands at 275 and 1052 cm^{-1} indicate that CuO NPs and ZnO NPs exist in the pores of mesoporous silica.

For detecting the distribution of metal oxides in mesoporous silica, Raman scanning was performed. Fig. 7a1, b1, and c1 show the photograph of the selected area of the samples SBA/CuO (a), SBA/ZnO (b) and SBA/CuZnO (c), which are presented with a grid (300 × 300 μm). Two points of Raman spectroscopy were taken from the red and blue regions (selected from Fig. 7a2, b2, and c2), and the result is shown at Fig. 7a3, b3, and c3. The result shows that both lines from red and blue regions display the peak of the metal oxide. Explain that the metal oxide was uniformly bonded to the mesoporous silicon frame.[46]

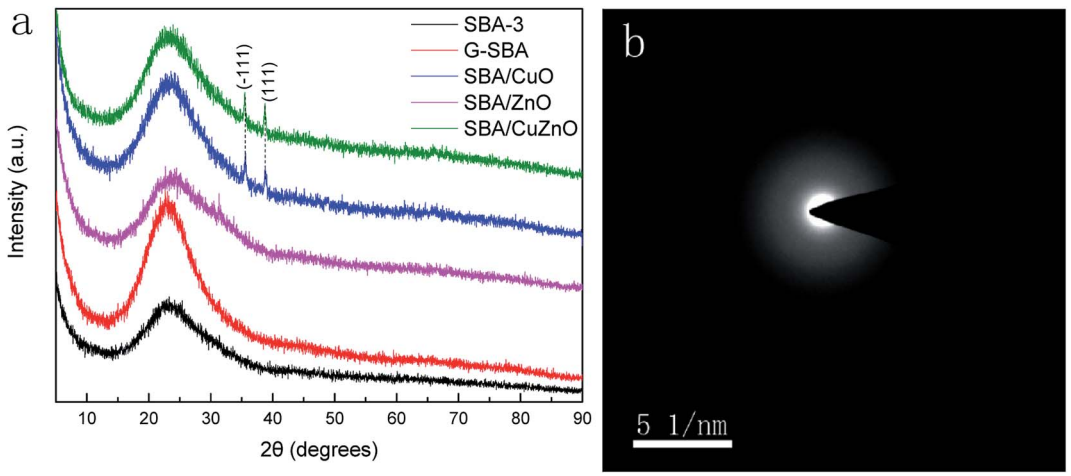

Fig. 5 WXRD of G-SBA, SBA/CuO, SBA/ZnO, and SBA/CuZnO (a) and SAED pattern of SBA/ZnO (b).

3.7. SEM analysis

Fig. 8 illustrates the SEM images of SBA-3 (a); G-SBA (b); SBA/CuO (c); SBA/ZnO (d) and SBA/CuZnO (e). Fig. 8 shows that the size of all mesoporous silica compositions is about 2 μm and distorted growth to near-spherical, which is closely related to pH during synthesis. Stronger is the acidity, higher is the order, and smaller is the size.[47] The surfaces of SBA-3 and G-SBA were smooth, indicating that the surface structure of mesoporous silica did not change after being modified with GLYMO–IDA. Compared to SBA-3, the surface of SBA/CuO, SBA/ZnO, and SBA/CuZnO become rough and possess a high ordered structure as SBA-3. The results from EDS of SBA-3; G-SBA; SBA/CuO; SBA/ZnO and SBA/CuZnO are provided in Fig. S1.† Compared to a2, a peak of C and N could be detected by EDS analysis, indicating that GLYMO–IDA was successfully modified in SBA-3. In c2, it shows the peak of Cu and its atomic percentage is 1.44%. The peak of Zn is showed in d2 and its atomic percentage is 1.19%. In e2, there are no peak showing Zn but showing a peak of Cu. Possibly because the content of Zn is below the detection limit of EDS, or the zinc oxide content on the mesoporous silicon surface is less.

3.8. TEM and HRTEM analysis

Fig. 9 depicts transmission electron microscopic (TEM) images of SBA-3, G-SBA, SBA/CuO, SBA/ZnO, and SBA/CuZnO and HRTEM images of SBA/CuO and SBA/CuZnO. The samples exhibit a typical mesoporous silica structure with long-range order, two dimensional hexagonal and honeycomb structure, which suggests that the introduction of organic functional groups and nano-metal oxides do not change the structure of

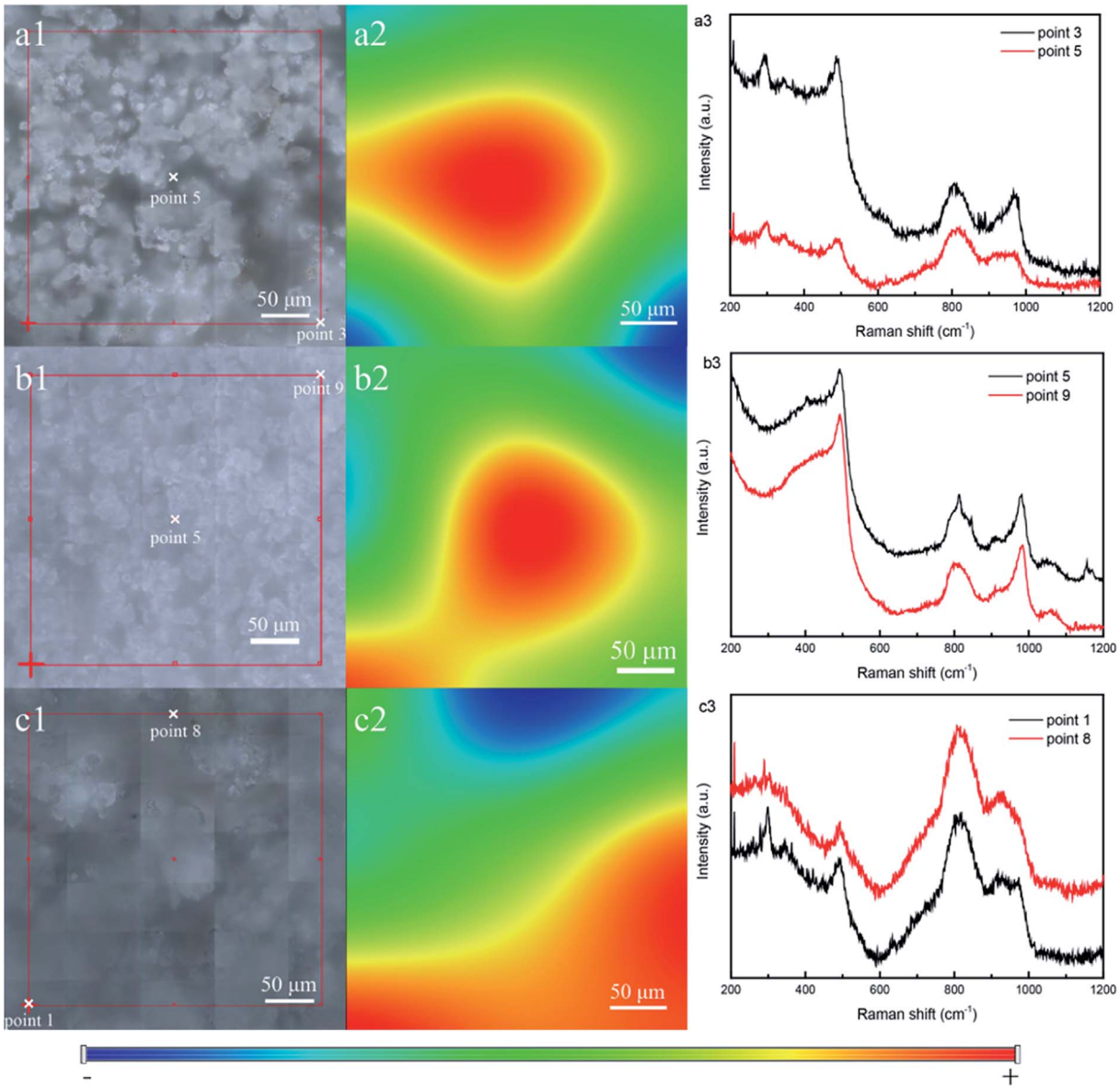

Fig. 7 Photograph of the selected area, Raman map and Raman spectra of SBA/CuO (a), SBA/ZnO (b) and SBA/CuZnO (c).

mesoporous silica. But the pore size (consistent with the results of BET analysis) and the interface distance between pores are changed. A series of uniform black dots can be observed in Fig. 9f and g. It refers to nano-metal oxide dispersion on the surface and shuttle in the pore channels of SBA-3. The average diameter of black dots (nano-CuO) in the Fig. 9f and black dots (nano-CuZnO) in the Fig. 9g were measured as 4.8 nm and 4.0 nm, respectively.

3.9. XPS analysis

Fig. 10 shows the XPS results of mesoporous silica for studying the composition and chemical bond configuration. In Fig. 10a, the lines of SBA/ZnO and SBA/Zn^{2+} display two obvious symmetrical binding energy regions at about 1022.0 eV and 1044.0 eV, attributing to Zn $2p_{3/2}$ and Zn $2p_{1/2}$.[20] For G-SBA/Zn^{2+}, two peaks are produced by zinc ions bound to GLYMO–IDA. After calcination to SBA/ZnO, the peak at 1021.7 eV shifted positively to 1022.6 eV, and the peak at 1044.9 eV shifted to 1045.6 eV; the distance between these two peaks was 23.0 eV, which agreed with the energy splitting value of ZnO,[48] because the difference in bond energy between the coordination and the ionic bond bounds to zinc. Conversely, the spectra of G-SBA/Cu^{2+}–Zn^{2+} and SBA/CuZnO displayed no obvious peak for Zn 2p, due to the lower load Zn^{2+} or ZnO at the SBA load bimetallic system. Table 3 shows that the loading of zinc ions on G-SBA/Cu^{2+}–Zn^{2+} and the loading of zinc oxide on SBA/CuZnO are only 0.19% and 0.13%, respectively. Fig. 10b shows two obvious peaks at about 933.0 eV and 932.0 eV, which are attributed to Cu $2p_{3/2}$ and Cu $2p_{1/2}$. The peak position of SBA/CuO and SBA/CuZnO showed a positive shift, compared to SBA/Cu^{2+} and SBA/Cu^{2+}–Zn^{2+}, because the coordination between GLYMO–IDA and copper ions has been disappeared after roasting. In addition, the low intensity shake up satellites for SBA/CuO and SBA/CuZnO might be due to *in situ* reduction of Cu(II) into Cu(I) during XPS analysis. Such *in situ* reduction could be due to the photoelectrons emitted from the materials.[49,50]

As for Fig. 10c, all the peaks of O 1s can form some peaks through separation. The spectral binding energy of other atoms shifted differently due to the functional modification of GLYMO–IDA or loaded ZnO. For G-SBA/Zn^{2+}, G-SBA/Cu^{2+} and G-SBA/Cu^{2+}–Zn^{2+}, the energy peaks negative-shifted from 532.9 eV to 532.3 eV, as GLYMO–IDA disturbed the electron distribution. For SBA/CuO, SBA/ZnO and SBA/CuZnO, the electron-donating ability of Zn/Cu, Si, and H were Zn/Cu > Si > H.[36] In addition, the electron intensity of O 1s of mesoporous silica supported metal oxide enhanced owing to the sacrifice of GLYMO–IDA and formation of metal oxide. In Fig. 10d, Si $2p_{3/2}$ centered at 104.1 $\pm$ 0.8 eV assigned to SiO_2.[51]

Fig. 10e exhibits the spectrum line of N 1s. The N 1s peaks show two components centered at 400.1 eV and 402.7 eV corresponding to the C–N and N–H from G-SBA, G-SBA/Cu^{2+}, G-SBA/Zn^{2+} and G-SBA/Cu^{2+}–Zn^{2+}.[52] Therefore, the coordination between the GLYMO–IDA and metal ions were successfully formed. After roasting, the peak at 402.7 eV disappeared and the peak at 400.1 eV became smaller because GLYMO–IDA decomposed after calcination in a muffle furnace. Fig. 10f shows the spectrum line of C 1s. The C 1s peaks of G-SBA, G-SBA/Cu^{2+}, G-SBA/Zn^{2+} and G-SBA/Cu^{2+}-Zn^{2+} show four components centered at 284.8 eV, 286.0 eV, 286.6 eV and 288.8 eV corresponding to the C–C and C–N, C–O and C=O.[53] The overall spectrums of SBA-3, G-SBA, SBA/CuO, SBA/ZnO, SBA/CuZnO; G-SBA/Cu^{2+}, G-SBA/Zn^{2+} and G-SBA/Cu^{2+}–Zn^{2+} are shown.

3.10. ICP-OES analysis

For determining the total content of metal oxides in all samples and the ability of mesoporous silica to support metal atoms before and after modification, further characterization was performed using ICP OES. Table 4 shows the mass ratio of Zn

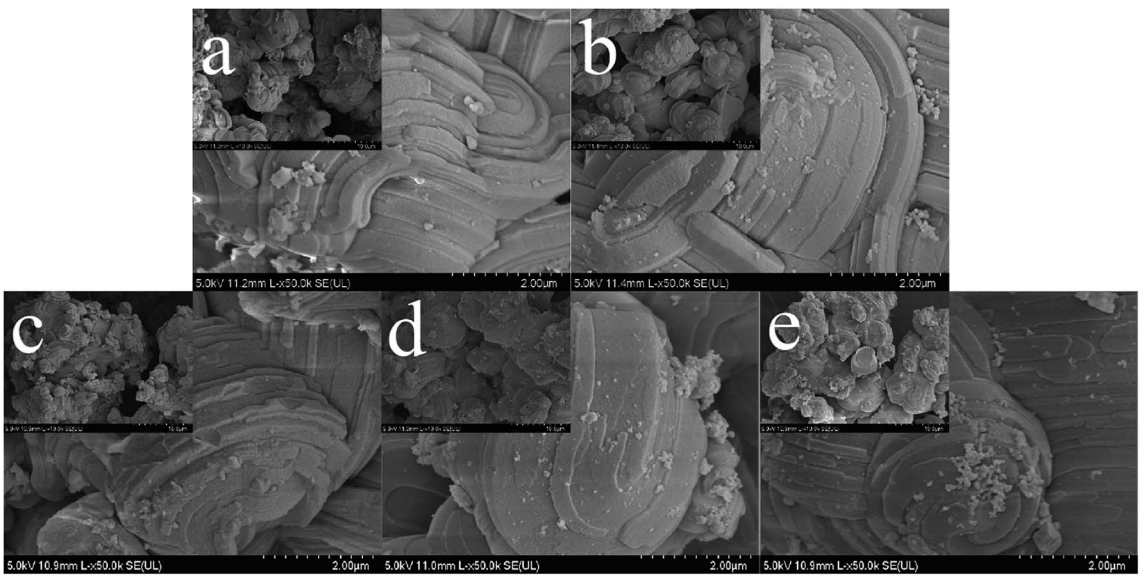

Fig. 8 Scanning Electron Microscope (SEM) of SBA-3 (a); G-SBA (b); SBA/CuO (c); SBA/ZnO (d) and SBA/CuZnO (e) (the scale in the small picture is 10 μm).

and Cu elements in SBA-3 supported metal ions (SBA-3/Zn^{2+}, SBA-3/Cu^{2+}, SBA-3/Cu^{2+}–Zn^{2+}), modified mesoporous silica-supported metal ions (G-SBA/Zn^{2+}, G-SBA/Cu^{2+}, G-SBA/Cu^{2+}–Zn^{2+}) and modified mesoporous silica-supported metal oxide (SBA/ZnO, SBA/CuO, SBA/CuZnO). Obviously, the amount of the modified mesoporous silica-supported metal ions was much

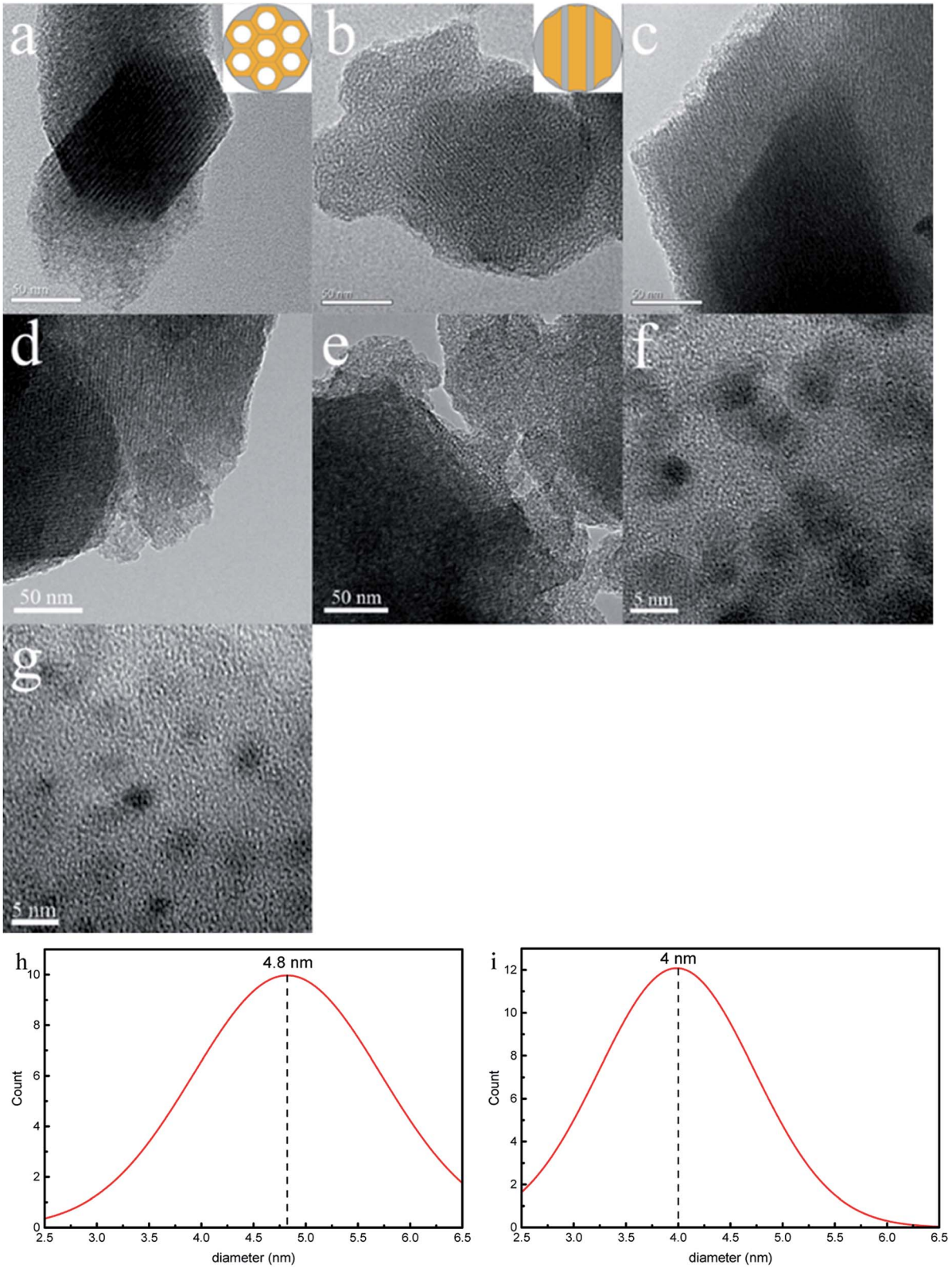

Fig. 9 Transmission electron microscopic (TEM) images of SBA-3 (a); G-SBA (b); SBA/CuO (c) SBA/ZnO (d) and SBA/CuZnO (e). HRTEM images of SBA/CuO (f); SBA/CuZnO (g) and the diameter distribution of nano-CuO (h) and nano-CuZnO (i).

higher than that of the unmodified mesoporous silica, indicating that GLYMO–IDA coordinated with the metal ions. The mass ratios of Zn element in SBA-3/Zn^{2+}, G-SBA/Zn^{2+} and SBA/ZnO are 0.37 ± 0.0062%, 2.21 ± 0.0540% and 2.48 ± 0.0610%, respectively, and the mass ratios of Cu element in SBA-3/Cu^{2+}, G-SBA/Cu^{2+} and SBA/CuO are 0.03 ± 0.0032%, 2.10

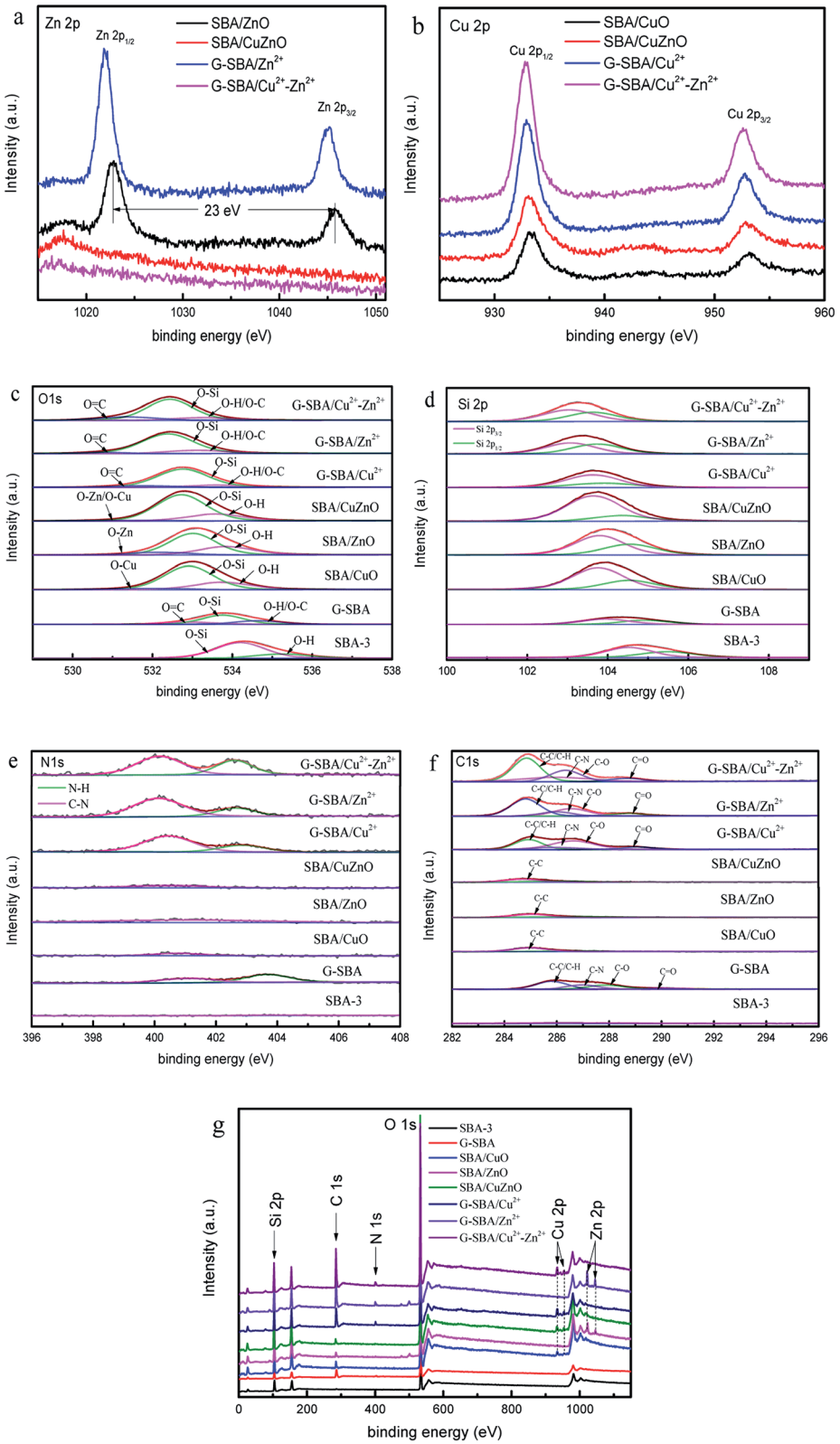

Fig. 10 X-ray photoelectron spectroscopy (XPS) of Zn 2p (a); Cu 2p (b); O 1s (c); Si 2p (d); N 1s (e); C 1s (f) the survey of SBA-3, G-SBA, SBA/CuO, SBA/ZnO, SBA/CuZnO; G-SBA/Cu^{2+}, G-SBA/Zn^{2+} and G-SBA/Cu^{2+}–Zn^{2+} (g).

Table 3 The binding energy and atomic energy of SBA-3, G-SBA, SBA/CuO, SBA/ZnO, SBA/CuZnO; G-SBA/Cu^{2+}, G-SBA/Zn^{2+} and G-SBA/Cu^{2+}–Zn^{2+}

	BE/eV						Atomic/%	
Material	Zn $2p_{1/2}$	Cu $2p_{1/2}$	O 1s	Si 2p	N 1s	C 1s	Zn 2p	Cu 2p
SBA-3	—	—	534.3	105.0	—	286.8	—	—
G-SBA	—	—	533.9	104.3	403.6	286.8	—	—
SBA/CuO	—	933.2	533.0	104.0	400.5	285.0	—	0.73
SBA/ZnO	1022.7	—	533.1	104.0	401.4	285.0	1.06	—
SBA/CuZnO	1017.5	933.1	532.8	103.8	400.6	284.8	0.13	0.87
G-SBA/Cu^{2+}	—	932.9	532.5	103.5	400.3	285.2	—	1.62
G-SBA/Zn^{2+}	1021.8	—	532.4	103.4	400.2	285.0	1.47	—
G-SBA/Cu^{2+}–Zn^{2+}	1016.9	932.8	532.4	103.3	400.2	285.0	0.19	1.53

$\pm$ 0.0480% and 2.43 $\pm$ 0.0550%, respectively. In loaded bimetallic systems, the mass ratio of Zn and Cu element in G-SBA/Cu^{2+}–Zn^{2+} are 0.12 $\pm$ 0.0083% and 2.25 $\pm$ 0.0360%, and the SBA/CuZnO was also followed this trend. The difference in mesoporous silica loading is observed because the competitive adsorption capacity of Cu^{2+} is greater.[54]

3.11. UV-vis spectroscopic analysis

It well known that the IDA-functionalized ligand has more affinity towards Cu^{2+} than Zn^{2+} ions and therefore the loaded of CuO into/onto silica is expected to be higher than that of ZnO-vis spectroscopic studies were conducted for obtaining the information regarding the state of ZnO, CuO and CuZnO NPs in the silica matrix (Fig. 11). At wavelengths from 200 nm to 400 nm, all of the samples displayed obvious absorption peaks. For SBA/ZnO, the band around 273 nm was attributed to the encapsulated zinc-oxide nanoparticles, indicating that most of the ZnO NPs were incorporated into the silica matrix of pore walls.[55] The bands between 264–350 nm in the curve of SBA/CuO were considered as the charge transfer transition from O^{2-} to Cu^{2+}.[56] In SBA/CuZnO, a red shift was observed in the absorption curve, indicating that the bimetallic oxides formed a nanocomposite in the channels of mesoporous silica, rather than being independent.[57,58]

Table 4 ICP-OES analysis of Zn content and Cu content in SBA composite material

Materials	Zn (wt%)	Cu (wt%)	Total (wt%)
SBA-3/Zn^{2+}	0.37 $\pm$ 0.0062	—	0.37 $\pm$ 0.0062
SBA-3/Cu^{2+}	—	0.03 $\pm$ 0.0032	0.03 $\pm$ 0.0032
SBA-3/Cu^{2+}–Zn^{2+}	0.06 $\pm$ 0.0035	0.03 $\pm$ 0.0021	0.09 $\pm$ 0.0056
G-SBA/Zn^{2+}	2.21 $\pm$ 0.0540	—	2.21 $\pm$ 0.0540
G-SBA/Cu^{2+}	—	2.10 $\pm$ 0.0480	2.10 $\pm$ 0.0480
G-SBA/Cu^{2+}–Zn^{2+}	0.12 $\pm$ 0.0083	2.25 $\pm$ 0.0360	2.37 $\pm$ 0.0443
SBA/ZnO	2.48 $\pm$ 0.0610	—	2.48 $\pm$ 0.0610
SBA/CuO	—	2.43 $\pm$ 0.0550	2.43 $\pm$ 0.0550
SBA/CuZnO	0.14 $\pm$ 0.0037	2.29 $\pm$ 0.0590	2.43 $\pm$ 0.0627

3.12. TGA and DTG analysis

Fig. 12 shows the thermogravimetric (TGA) and DTG curves of SBA-3 (a), G-SBA (b), G-SBA/Cu^{2+} (c), G-SBA/Zn^{2+} (d) and G-SBA/Cu^{2+}–Zn^{2+} (e). At 40–150 °C, the weight loss of all the samples was assigned to the loss of the water. The second weight loss of SBA-3 (4.9%) was due to the loss of the hydroxyl groups.[59] For G-SBA, G-SBA/Cu^{2+}, G-SBA/Zn^{2+} and G-SBA/Cu^{2+}–Zn^{2+}, a more significant second weight loss can be observed (18.6%, 16.1%, 16.6% and 14.3% respectively), resulting in the loss of the organic groups from GLYMO–IDA. So, the organic functional groups were successfully incorporated into the mesoporous silica matrix.

3.13. Antibacterial assays

Fig. 13 shows the images of the antibacterial studies of SBA-3, SBA/CuO, SBA/ZnO, and SBA/CuZnO at different concentrations. The degree of antibacterial activity was different for both types of bacteria and NPs. The picture depicts that the mesoporous silica SBA-3 has imparted very weak sterilization effect on both bacteria due to the adsorption of mesoporous silica. As for *E. coli*, SBA/CuO shows the best bacteriostatic effect, reaching to 85.87% (as shown in Fig. 13i) at a concentration of

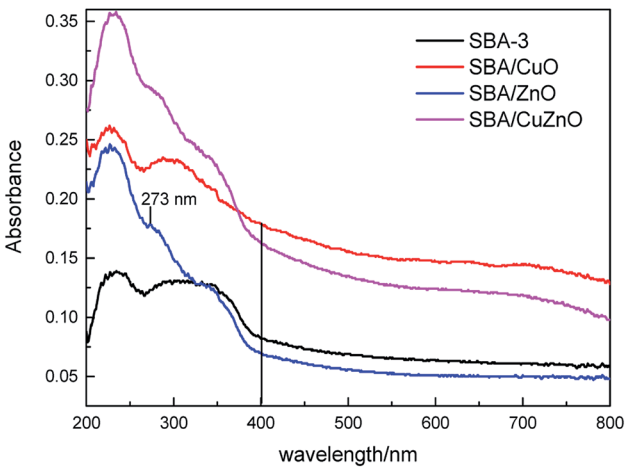

Fig. 11 UV-vis DRS of SBA-3, SBA/CuO, SBA/ZnO, and SBA/CuZnO.

250 ppm. The inhibition rate of SBA/CuZnO is 67.39%. SBA/ZnO showed a poor bacteriostatic performance with the inhibition rate of 32.61%. Against *S. aureus*, the order of antibacterial potential was SBA/CuO > SBA/CuZnO > SBA/ZnO, and the bacteriostatic rate reached to 100%, 100%, and 38.33%, respectively at 250 ppm concentration, because the SBA/CuO and SBA/CuZnO had a {111} lattice plane (Fig. 5), which enhanced the bactericidal effect of nano-copper oxide.[60] This result was consistent with results of other studies regarding metal oxide sterilization.[61] The antibacterial activity of all the complexes against *S. aureus* was higher than *E. coli* because the cell wall structure of *S. aureus* was simple and easily destroyed. While the cell wall of *E. coli* displayed three layers, those blocked the destruction of cell walls by metal oxides.[62] Anna Donnadio[26] reported the antibacterial and fungal properties of mesoporous silicon-loaded nano zinc oxide. It shows that most of the prepared composites resulted active against both bacteria and fungi. Hongjian Wen[36] prepares PEI-coated mesoporous silicon to adsorb zinc ions and roasted into zinc oxide. ZnO–SBA-15s suppressed the growth of *E. coli* compared to blank SBA-15 in a ZnO dose-dependent manner.

Fig. 14 shows the images of the antibacterial studies of SBA/CuO, SBA + CuO, SBA/ZnO, SBA + ZnO, SBA/CuZnO and SBA + CuZnO against *E. coli* and *S. aureus* (sample concentration is 250 ppm). GLYMO–IDA modified mesoporous silica-supported nano-metal oxide exhibited excellent antibacterial properties

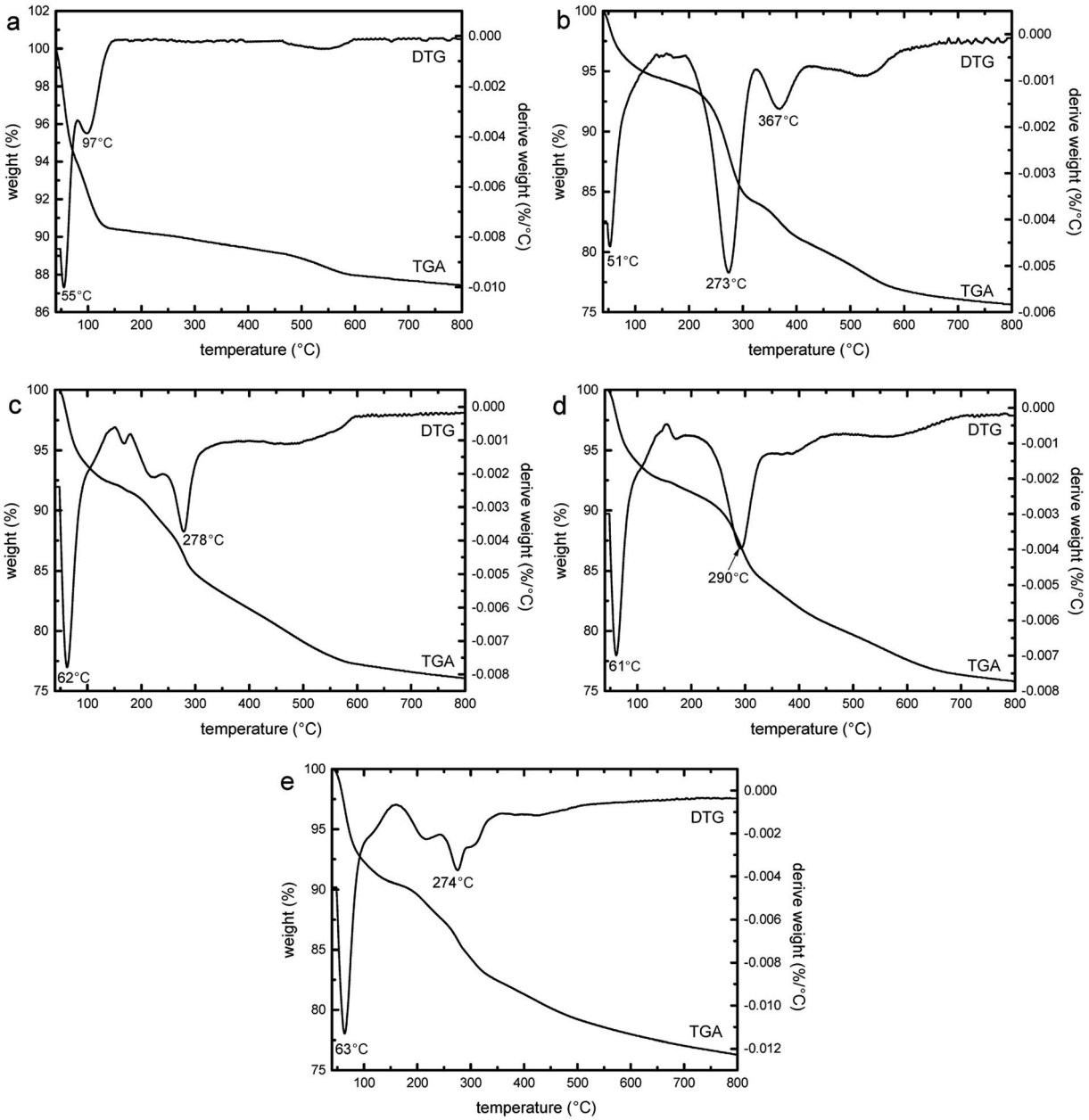

Fig. 12 Thermogravimetric (TGA) and DTG curves of SBA-3 (a), G-SBA (b), G-SBA/Cu^{2+} (c), G-SBA/Zn^{2+} (d) and G-SBA/Cu^{2+}–Zn^{2+} (e).

against both bacteria compared to the commercial nano-oxides. Two important factors must be considered: (1) the size of nano-metal oxide in the pores of mesoporous silica was smaller than commercial nano-oxides; (2) mesoporous silica exhibited good dispersive ability to nano-metal oxides, so that the nano-metal oxide could be uniformly dispersed on the inner and outer

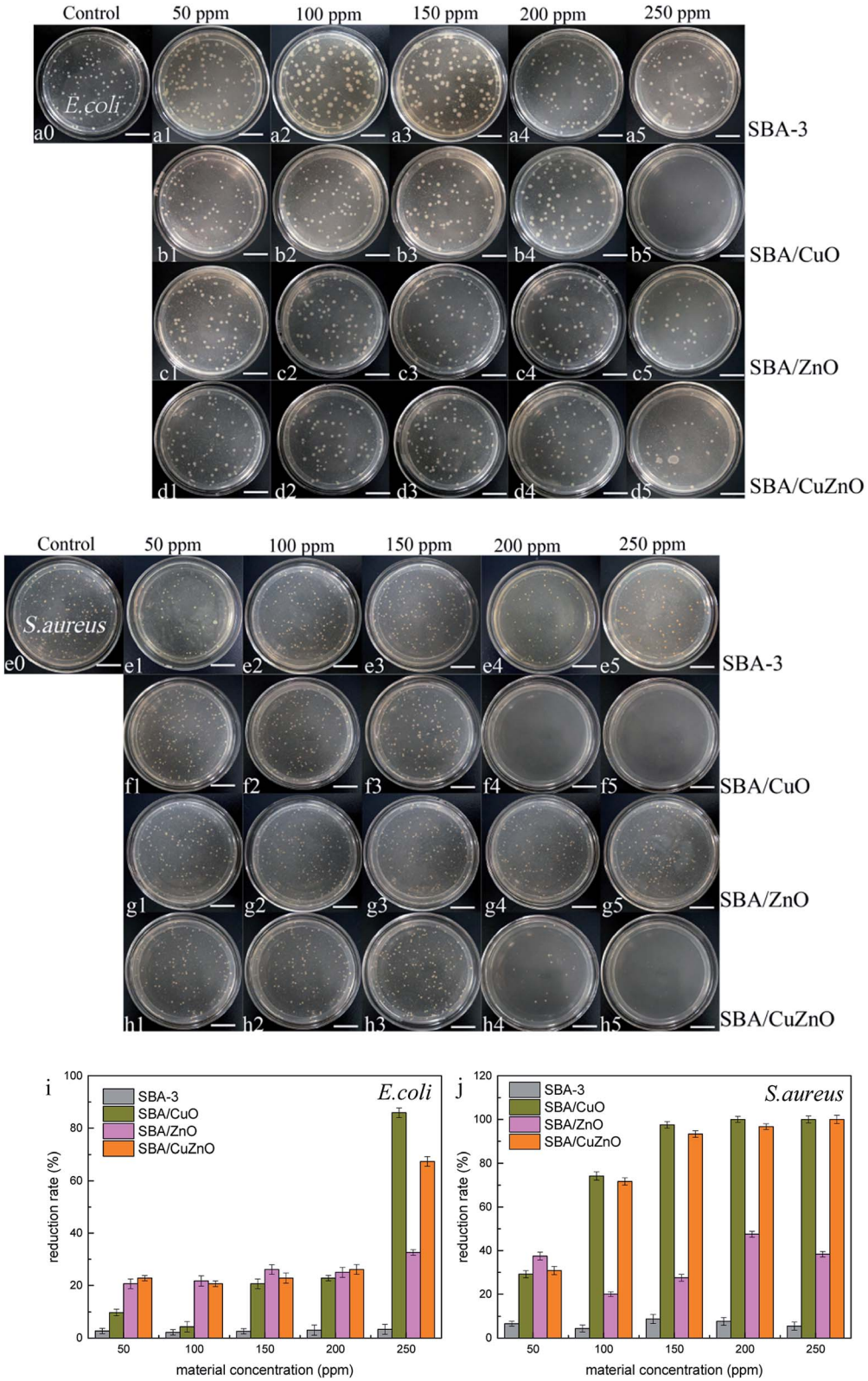

Fig. 13 Images of the antibacterial assays of SBA, SBA/CuO, SBA/ZnO and SBA/CuZnO at different concentrations inhibit *E. coli* (a–d) and *S. aureus* (e–h) (the scale in the picture is 20 μm). Their antibacterial reduction rate with *E. coli* (i) and *S. aureus* (j).

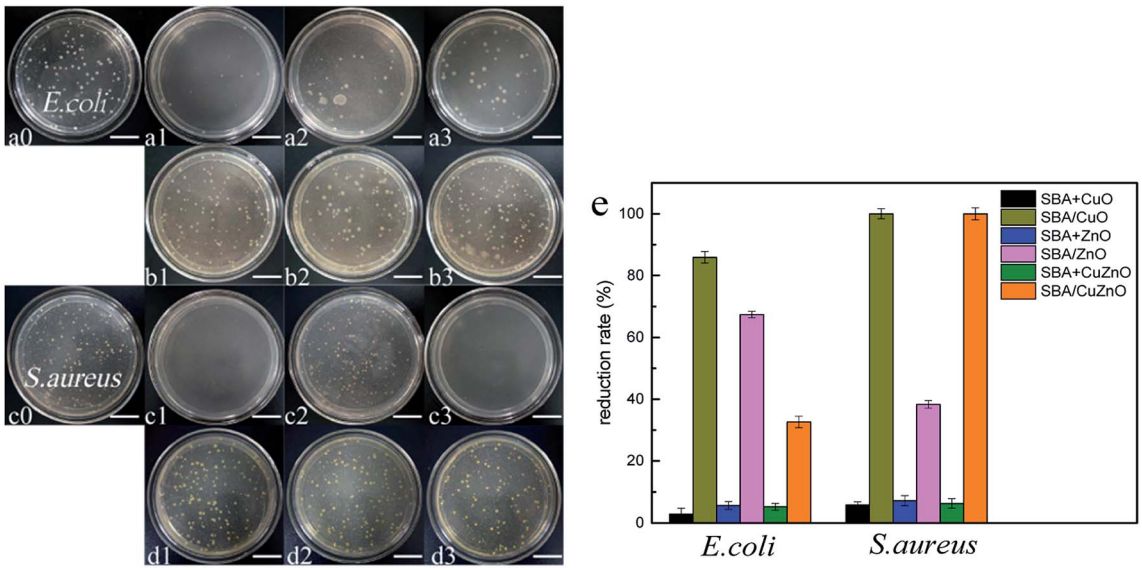

Fig. 14 Images of the antibacterial assays of SBA/CuO (a1 and c1), SBA + CuO (b1 and d1), SBA/ZnO (a2 and c2), SBA + ZnO (b2 and d2), SBA/CuZnO (a3 and c3) and SBA + CuZnO (b3 and d3) inhibit *E. coli* (a and b) and *S. aureus* (c and d) (the scale in the picture is 20 μm). Their antibacterial reduction rate with *E. coli* and *S. aureus* (e).

surfaces of mesoporous silica. In Fig. 14e, their antibacterial reduction rate showed that antibacterial ability of mesoporous silica supported metal oxide was several times higher than mesoporous silica mixing metal oxide at the same metal oxide concentration.

3.14. MIC and MBC determination

Tables 5 and 6 have summarized the MIC and MBC of SBA/CuO, SBA/ZnO and SBA/CuZnO. The growth of *E. coli* bacteria was inhibited at higher concentrations of SBA/CuO, SBA/ZnO, and SBA/CuZnO mesoporous silica composite compared to Gram-positive bacteria, which agreed with the reports of Z. Emami-Karvani *et al.*,[63] where the MIC and MBC of pure ZnO (the size was 3 nm) were 1 and 16 mg mL^{-1} inhibit *E. coli* and 0.5 and 8 mg mL^{-1} inhibit *S. aureus*. The MIC and MBC of pure copper oxide in the article[64] were 5.2 and 8.1 mg mL^{-1} inhibit *E. coli*, and 4.5 and 7 mg mL^{-1} inhibit *S. aureus*. Compared to that study, mesoporous silica-supported metal oxide systems exhibited lower MIC and MBC, which was 0.304 and 1.215 mg mL^{-1} for SBA/CuO inhibit *E. coli*, and 0.076 and 0.6075 mg mL^{-1} inhibit *S. aureus*. When SBA/ZnO inhibited *E. coli*, the MIC and MBC were 1.24 and >2.48 mg mL^{-1}, and 0.31 and >2.48 mg mL^{-1} inhibit *S. aureus*. The MIC and MBC of SBA/CuZnO were higher than copper oxide but lower than zinc oxide because the dispersion of mesoporous silica allowed the metal oxide to be evenly distributed in the pores in a smaller size. Many studies have shown that the size of nano-metal oxides significantly influenced their antibacterial properties. Smaller was the size, better was the antibacterial efficacy.[65,66]

3.15. Antibacterial mechanism analysis

Normally, the mechanism of the antibacterial property of metal oxide is explained by the release of dissociated metal ions and the release of reactive oxygen species (ROS). This study elucidated the antibacterial mechanism (as shown in Fig. 15) by measuring the production of hydrogen peroxide under UV light.

Fig. 16a depicted the absorbance of H_2O_2 in different suspension under ultraviolet light. SBA-3 and G-SBA did not produce H_2O_2, while SBA/CuO, SBA/ZnO, and SBA/CuZnO showed a strong absorbance at 570 nm. Greater absorbance suggests the formation of more hydrogen peroxide by the composite material, which indicates that the SBA/CuZnO can generate the maximum amount of hydrogen peroxide under ultraviolet light. This result also showed that the photocatalytic performance of the mesoporous silica-loaded bimetallic system

Table 5 Determination of MIC of the samples inhibit *E. coli* and *S. aureus*

	MIC (mg mL^{-1})					
Strains	SBA/CuO	CuO	SBA/ZnO	ZnO	SBA/CuZnO	CuZnO
E. coli	12.5	0.304	50	1.24	25	0.558
S. aureus	3.125	0.076	12.5	0.31	6.25	0.139

Table 6 Determination of MBC of the samples against *E. coli* and *S. aureus*

	MBC (mg mL^{-1})					
Strains	SBA/CuO	CuO	SBA/ZnO	ZnO	SBA/CuZnO	CuZnO
E. coli	50	1.215	>100	>2.48	100	2.23
S. aureus	25	0.6075	>100	>2.48	50	1.115

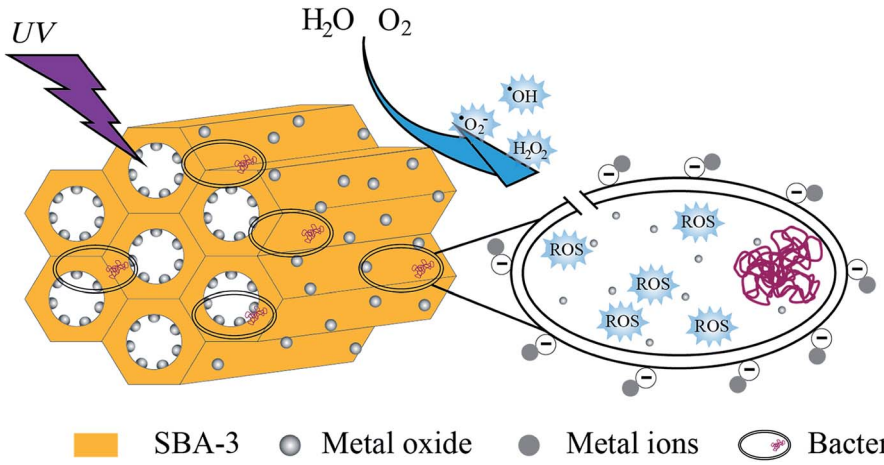

Fig. 15 Schematic representation of hypothetical antibacterial mechanism of mesoporous silica supported metal oxide composites.

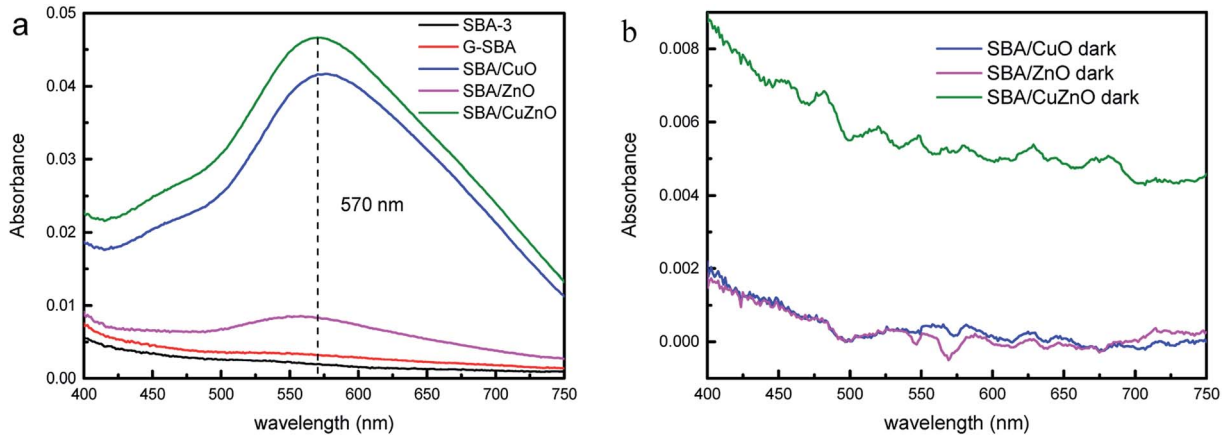

Fig. 16 Absorbance variation of production of H_2O_2 in different suspension under ultraviolet light (a) and in dark (b).

was improved in the ultraviolet region (consistent with the results of Fig. 11).

Fig. 16b shows the absorbance of H_2O_2 in different suspension in dark. SBA/CuO, SBA/ZnO, and SBA/CuZnO demonstrated almost no absorption peak at 570 nm, indicating that UV light promoted the production of hydrogen peroxide and improved the bactericidal properties of the material.

Table 7 listed the ICP-OES analysis of Zn and Cu in SBA loaded metal oxide. After UV treatment, the total metal content released in the samples was basically the same as the total metal element released in the dark. In addition, the release of zinc was around three times that of copper. This result indicates that ultraviolet irradiation enhances the bactericidal effect by increasing the formation of hydrogen peroxide, rather than increasing the release of the metal elements. Among the antibacterial results of antibacterial activity, SBA/CuO displayed the best antibacterial properties. Although the H_2O_2 production and metal ion leaching were the lowest, the best antibacterial properties were obtained from the high-atom-density {111} facets.[65]

3.16. Photocatalytic antibacterial assays

Fig. 17 shows images of the photocatalytic antibacterial assays of SBA/CuO, SBA/ZnO, and SBA/CuZnO at 150 ppm against *S. aureus*. The antibacterial activity of all the samples was increased after UV treatment, among which SBA/CuZnO was the best, suggesting that the ultraviolet light could improve the antibacterial properties of mesoporous silica supported metal oxides (SBA/CuO, SBA/ZnO, and SBA/CuZnO), which was consistent with the results of UV-vis diffuse reflectance spectral

Table 7 ICP-OES analysis of Zn content and Cu content in SBA loaded metal oxide

Materials	Zn (ppm)	Cu (ppm)	Total (ppm)
SBA/ZnO + UV light	0.644 ± 0.005	—	0.644 ± 0.005
SBA/CuO + UV light	—	0.216 ± 0.011	0.216 ± 0.011
SBA/CuZnO + UV light	0.308 ± 0.012	0.195 ± 0.018	0.503 ± 0.030
SBA/ZnO + dark	0.550 ± 0.011	—	0.550 ± 0.011
SBA/CuO + dark	—	0.217 ± 0.009	0.217 ± 0.009
SBA/CuZnO + dark	0.316 ± 0.008	0.199 ± 0.006	0.515 ± 0.014

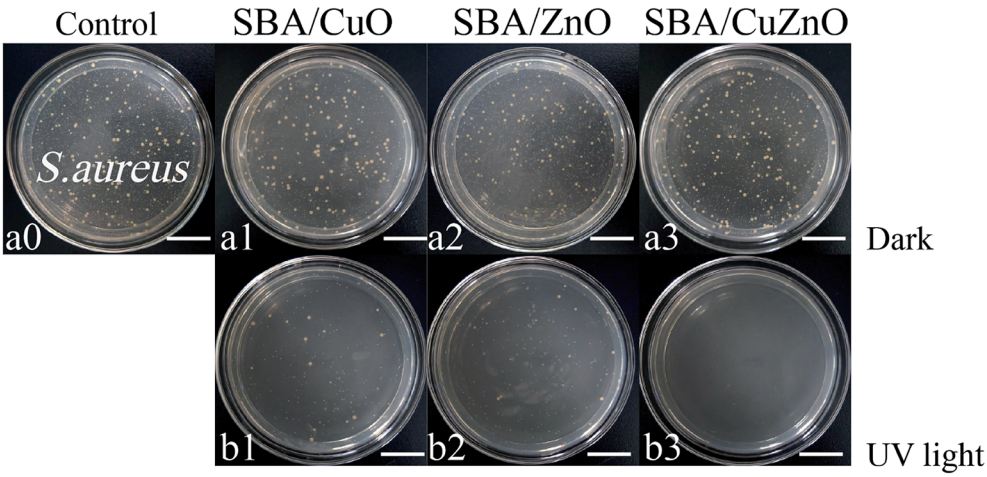

Fig. 17 Images of the photocatalytic antibacterial assays of SBA/CuO, SBA/ZnO and SBA/CuZnO with 150 ppm against *S. aureus* (a and b) (the scale in the picture is 20 μm).

analysis. The underlying mechanism could be explained by the suppression of the electron–hole recombination among the composite of SBA/CuZnO, leading to high photocatalytic efficiency.[29] Furthermore, photocatalytic antibacterial properties of SBA/CuZnO may be attributed to cell permeability alteration.[31] The photocatalytic antibacterial properties of bimetallic oxides can be effectively applied in water disinfection, food packaging, coating and sewage treatment.[67]

4. Conclusion

Mesoporous silica can greatly increase the loading of the metal ions by simple GLYMO–IDA modification. The nano-particles of calcined metal oxide was successfully loaded onto the mesoporous silica and uniformly distributed. The antibacterial performance of mesoporous silica-loaded bimetallic system in the absence of light is not as good as that of mesoporous silica-supported copper oxide. Under ultraviolet light, the bimetallic system exhibits superior antibacterial properties. After the dispersion of mesoporous silica, the antibacterial properties of the nano-metal oxide were improved, and both the MIC and the MBC were decreased. This non-toxic antibacterial material can be widely used in various fields, such as packaging materials, feed additives, preservatives, *etc.*

Conflicts of interest

The authors declare no competing financial interest.

Acknowledgements

This research was funded by National Natural Science Foundation of China (grant no. 21576303), Natural Science Foundation of Guangdong Province (grant no. 2017A030311003), Science and Technology Program of Guangzhou, China (grant no. 201903010011, 201604020074), Innovation Team of Modern Agricultural Industry Technology System of Guangdong Province (2019KJ140) and College Students Innovation and Entrepreneurship Training Program (201811347002, S201911347022).

References

1 X. He, D. P. Yang, X. Zhang, M. Liu, Z. Kang, C. Lin, N. Jia and R. Luque, Waste eggshell membrane-templated CuO–ZnO nanocomposites with enhanced adsorption, catalysis and antibacterial properties for water purification, *Chem. Eng. J.*, 2019, **369**, 621–633.

2 D. Malwal and P. Gopinath, Efficient adsorption and antibacterial properties of electrospun CuO–ZnO composite nanofibers for water remediation, *J. Hazard. Mater.*, 2017, **321**, 611–621.

3 J. Huang, L. Lin, D. Sun, H. Chen, D. Yang and Q. Li, Bio-inspired synthesis of metal nanomaterials and applications, *Chem. Soc. Rev.*, 2015, **44**, 6330–6374.

4 R. J. B. Peters, H. Bouwmeester, S. Gottardo, V. Amenta, M. Arena, P. Brandhoff, H. J. P. Marvin, A. Mech, F. Botelho Moniz, L. Quiros Pesudo, H. Rauscher, R. Schoonjans, A. K. Undas, M. V. Vettori, S. Weigel and K. Aschberger, Nanomaterials for products and application in agriculture, feed and food, *Trends Food Sci. Technol.*, 2016, **54**, 155–164.

5 A. S. Prasad, Clinical, immunological, anti-inflammatory and antioxidant roles of zinc, *Exp. Gerontol.*, 2008, **43**, 370–377.

6 V. Holubnycha; M. Pogorielov; V. Korniienko; O. Kalinkevych; O. Ivashchenko; B. Peplinska and M. Jarek Antibacterial activity of the new copper nanoparticles and Cu NPs/chitosan solution, in, *2017 IEEE 7th international conference on nanomaterials: application &properties*, IEEE, 2017 pp. 04NB10-01–04NB10-04.

7 R. Raguvaran, A. Manuja and B. K. Manuja, Zinc oxide nanoparticles: opportunities and challenges in veterinary sciences, *Immunome Res.*, 2015, **11**, 95.

8 G. Suresh, R. K. Das, S. K. Brar, T. Rouissi, A. A. Ramirez, Y. Chorfi and S. Godbout, Alternatives to antibiotics in poultry feed: molecular perspectives, *Crit. Rev. Microbiol.*, 2018, **44**, 318–335.

9 M. Alagawany, M. E. Abd El-Hack, M. R. Farag, S. Sachan, K. Karthik and K. Dhama, The use of probiotics as eco-friendly alternatives for antibiotics in poultry nutrition, *Environ. Sci. Pollut. Res.*, 2018, **25**, 10611–10618.

10 J. Wang, X. Dou, J. Song, Y. Liu, X. Zhu, L. Xu, W. Li and A. Shan, Antimicrobial peptides: promising alternatives in the post feeding antibiotic era, *Med. Res. Rev.*, 2018, **39**, 831–859.

11 W. H. Kim and H. S. Lillehoj, Immunity, immunomodulation, and antibiotic alternatives to maximize the genetic potential of poultry for growth and disease response, *Anim. Feed Sci. Technol.*, 2019, **250**, 41–50.

12 M. Alavi and M. Rai, Recent advances in antibacterial applications of metal nanoparticles (MNPs) and metal nanocomposites (MNCs) against multidrug-resistant (MDR) bacteria, *Expert Rev. Anti-Infect. Ther.*, 2019, **217**, 419–428.

13 A. Sirelkhatim, S. Mahmud, A. Seeni, N. H. M. Kaus, L. C. Ann, S. K. M. Bakhori, H. Hasan and D. Mohamad, Review on zinc oxide nanoparticles: antibacterial activity and toxicity mechanism, *Nano-Micro Lett.*, 2015, **7**, 219–242.

14 S. Meghana, P. Kabra, S. Chakraborty and N. Padmavathy, Understanding the pathway of antibacterial activity of copper oxide nanoparticles, *RSC Adv.*, 2015, **5**, 12293–12299.

15 A. Fakhri, M. Azad and S. Tahami, Degradation of toxin *via* ultraviolet and sunlight photocatalysis using ZnO quantum dots/CuO nanosheets composites: preparation and characterization studies, *J. Mater. Sci.: Mater. Electron.*, 2017, **28**, 16397–16402.

16 M. A. Subhan, N. Uddin, P. Sarker, A. K. Azad and B. Kulsuma, Photoluminescence, photocatalytic and antibacterial activities of $CeO_2 \cdot CuO \cdot ZnO$ nanocomposite fabricated by co-precipitation method, *Spectrochim. Acta, Part A*, 2015, **149**, 839–850.

17 J. Wang, T. Tsuzuki, B. Tang, P. Cizek, L. Sun and X. Wang, Synthesis of silica-coated ZnO nanocomposite: the resonance structure of polyvinyl pyrrolidone (PVP) as a coupling agent, *Colloid Polym. Sci.*, 2010, **288**, 1705–1711.

18 F. Hoffmann, M. Cornelius, J. Morell and M. Fröba, Silica-based mesoporous organic–inorganic hybrid materials, *Angew. Chem., Int. Ed.*, 2006, **45**, 3216–3251.

19 E. Da'Na, Adsorption of heavy metals on functionalized-mesoporous silica: a review, *Microporous Mesoporous Mater.*, 2017, **247**, 145–157.

20 Z. Shen, H. Zhou, H. Chen, H. Xu, C. Feng and X. Zhou, Synthesis of nano-zinc oxide loaded on mesoporous silica by coordination effect and its photocatalytic degradation property of methyl orange, *Nanomaterials*, 2018, **8**, 317.

21 I. M. El-Nahhal, F. S. Kodeh, J. K. Salem, T. Hammad, S. Kuhn, R. Hempelmann and S. A. Bhaisi, Silica, Mesoporous Silica and Its Thiol Functionalized Silica Coated MgO and $Mg(OH)_2$ Materials, *Chemistry Africa*, 2019, **2**, 267–276.

22 R. Malhotra and A. Ali, 5-Na/ZnO doped mesoporous silica as reusable solid catalyst for biodiesel production *via* transesterification of virgin cottonseed oil, *Renewable Energy*, 2019, **133**, 606–619.

23 Y. Tian, J. Qi, W. Zhang, Q. Cai and X. Jiang, Facile, one-pot synthesis, and antibacterial activity of mesoporous silica nanoparticles decorated with well-dispersed silver nanoparticles, *ACS Appl. Mater. Interfaces*, 2014, **6**, 12038–12045.

24 D. Maučec, A. Šuligoj, A. Ristić, G. Dražić, A. Pintar and N. N. Tušar, Titania *versus* zinc oxide nanoparticles on mesoporous silica supports as photocatalysts for removal of dyes from wastewater at neutral pH, *Catal. Today*, 2018, **310**, 32–41.

25 M. Rajabzadeh, R. Khalifeh, H. Eshghi and M. Sorouri, Design and preparation of hallow mesoporous silica spheres include CuO and its catalytic performance for synthesis of 1,2,3-triazole compounds *via* the click reaction in water, *Catal. Lett.*, 2019, **149**, 1125–1134.

26 A. Donnadio, G. Cardinali, L. Latterini, L. Roscini and V. Ambrogi, Nanostructured zinc oxide on silica surface: preparation, physicochemical characterization and antimicrobial activity, *Mater. Sci. Eng. C*, 2019, **104**, 109977.

27 D. Zhang, Synthesis and characterization of ZnO-doped cupric oxides and evaluation of their photocatalytic performance under visible light, *Transition Met. Chem.*, 2010, **35**, 689–694.

28 D. Zhang and F. Zeng, Structural, photochemical and photocatalytic properties of zirconium oxide doped TiO_2 nanocrystallites, *Appl. Surf. Sci.*, 2010, **257**, 867–871.

29 A. Samad, M. Furukawa, H. Katsumata, T. Suzuki and S. Kaneco, Photocatalytic oxidation and simultaneous removal of arsenite with CuO/ZnO photocatalyst, *J. Photochem. Photobiol., A*, 2016, **325**, 97–103.

30 R. He, Z. Wang, L. Tan, Y. Zhong, W. Li, D. Xing, C. Wei and Y. Tang, Design and fabrication of highly ordered ion imprinted SBA-15 and MCM-41 mesoporous organosilicas for efficient removal of Ni^{2+} from different properties of wastewaters, *Microporous Mesoporous Mater.*, 2018, **257**, 212–221.

31 X. Li, Y. Che, Y. Lv, F. Liu, Y. Wang, C. Zhao and C. Liu, Synthesis and characterization of CuZnO@GO nanocomposites and their enhanced antibacterial activity with visible light, *J. Sol. Gel Sci. Technol.*, 2018, **89**, 672–684.

32 Q. Yu, X. Xu, C. Wang, Y. Ma, D. Hui and Z. Zhou, Remarkably improvement in antibacterial activity by synergistic effect in n-Cu@T–ZnO nanocomposites, *Composites, Part B*, 2017, **110**, 32–38.

33 L. L. Duffy, M. J. Osmond-Mcleod, J. Judy and T. King, Investigation into the antibacterial activity of silver, zinc oxide and copper oxide nanoparticles against poultry-relevant isolates of Salmonella and Campylobacter, *Food Control*, 2018, **92**, 293–300.

34 H. Ma, Q. Li, Y. Shi and X. Sun, Ni_2P/ZrO_2-SBA-15 dibenzothiophene hydrodesulfurization catalysts: preparation, characterization and evaluation, *Trans. Tianjin Univ.*, 2018, **24**, 340–350.

35 C. Airoldi and V. V. Oliveira, Hydrophobic contribution to amoxicillin release associated with organofunctionalized mesoporous SBA-16 carriers, *Mater. Res. Bull.*, 2014, **59**, 214–222.

36 H. Wen, X. Zhou, Z. Shen, Z. Peng, H. Chen, L. Hao and H. Zhou, Synthesis of ZnO nanoparticles supported on mesoporous SBA-15 with coordination effect-assist for antibacterial assessment, *Colloids Surf., B*, 2019, **181**, 285–294.

37 F. Boubekr, A. Davidson, S. Casale and P. Massiani, Ex-nitrate Co/SBA-15 catalysts prepared with calibrated silica grains: information given by TPR, TEM, SAXS and WAXS, *Microporous Mesoporous Mater.*, 2011, **141**, 157–166.

38 A. S. Maria Chong and X. S. Zhao, Functionalization of SBA-15 with APTES and characterization of functionalized materials, *J. Phys. Chem. B*, 2003, **107**, 12650–12657.

39 P. F. Fulvio, S. Pikus and M. Jaroniec, Tailoring properties of SBA-15 materials by controlling conditions of hydrothermal synthesis, *J. Mater. Chem.*, 2005, **15**, 5049–5053.

40 I. M. El-Nahhal, J. K. Salem, N. S. Tabasi, R. Hempelmann and F. S. Kodeh, Synthesis and structural characterization of ZnO-and CuO-NPs supported mesoporous silica materials (hexagonal SBA-15 and lamellar-SiO_2), *Chem. Phys. Lett.*, 2018, **691**, 211–218.

41 E. Janiszewska, M. Zieliński, M. Kot, E. Kowalewski and A. Śrębowata, Aqueous-phase hydrodechlorination of trichloroethylene on Ir catalysts supported on SBA-3 materials, *ChemCatChem*, 2018, **10**, 4109–4118.

42 V. Kampars, S. Zīriņa, A. Stanke, S. Agija and R. Modris, Fast pyrolysis of rapeseed oil in presence of CuO supported SBA-15 catalysts, *Key Eng. Mater.*, 2018, **762**, 141–145.

43 G. Hu, W. Li, J. Xu, G. He, Y. Ge, Y. Pan, J. Wang and B. Yao, Substantially reduced crystallization temperature of SBA-15 mesoporous silica in $NaNO_3$ molten salt, *Mater. Lett.*, 2016, **170**, 179–182.

44 W. Shen, D. Mao, Z. Luo and J. Yu, CO oxidation on mesoporous SBA-15 supported CuO–CeO_2 catalyst prepared by a surfactant-assisted impregnation method, *RSC Adv.*, 2017, **7**, 27689–27698.

45 M. Kahouli, A. Barhoumi, A. Bouzid, A. A. Hajry and S. Guermazi, Structural and optical properties of ZnO nanoparticles prepared by direct precipitation method, *Superlattices Microstruct.*, 2015, **85**, 7–23.

46 A. Popa, V. Sasca and I. Holclajtner-Antunović, The influence of surface coverage on textural, structural and catalytic properties of cesium salts of 12-molybdophosphoric acid supported on SBA-15 mesoporous sili*ca*, *Microporous Mesoporous Mater.*, 2012, **156**, 127–137.

47 M. V. Ponte, L. P. Rivoira, J. Cussa, M. L. Martínez, A. R. Beltramone and O. A. Anunziata, Optimization of the synthesis of SBA-3 mesoporous materials by experimental design, *Microporous Mesoporous Mater.*, 2016, **227**, 9–15.

48 X. Cai, D. Hu, S. Deng, B. Han, Y. Wang, J. Wu and Y. Wang, Isopropanol sensing properties of coral-like ZnO–CdO composites by flash preparation *via* self-sustained decomposition of metal–organic complexes, *Sens. Actuators, B*, 2014, **198**, 402–410.

49 M. C. Biesinger, Advanced analysis of copper X-ray photoelectron spectra, *Surf. Interface Anal.*, 2017, **49**, 1325–1334.

50 V. Di Castro and G. Piredda, Photoinduced reduction of silica supported CuO during XPS irradiation, *Chem. Phys. Lett.*, 1985, **114**, 109–113.

51 L. G. Gomes, A. G. Ferreira, C. M. Fernandes, D. S. W. Marcos, G. P. Lana, G. D. Assis, d. M. M. Coutinho, d. A. M. W. Augusto, N. M. Jose and B. d. S. E. Martins, Protection of normal cells from irradiation bystander effects by silica-flufenamic acid nanoparticles, *Mater. Med.*, 2018, **29**, 130.

52 I. M. El-Nahhal, M. Chehimi and M. Selmane, Synthesis and structural characterization of G – SBA-IDA, G-SBA-EDTA and G-SBA-DTPA modified mesoporous SBA-15 silica and their application for removal of toxic metal ions pollutants, *Silicon*, 2018, **10**, 981–993.

53 J. Deng, T. Wang, J. Guo and P. Liu, Electrochemical capacity fading of polyaniline electrode in supercapacitor: An XPS analysis, *Prog. Nat. Sci.: Mater. Int.*, 2017, **27**, 257–260.

54 L. Li, F. Liu, X. Jing, P. Ling and A. Li, Displacement mechanism of binary competitive adsorption for aqueous divalent metal ions onto a novel IDA-chelating resin: Isotherm and kinetic modeling, *Water Res.*, 2011, **45**, 1177–1188.

55 I. Trendafilova, A. Szegedi, J. Mihály, G. Momekov, N. Lihareva and M. Popova, Preparation of efficient quercetin delivery system on Zn-modified mesoporous SBA-15 silica carrier, *Mater. Sci. Eng. C*, 2017, **73**, 285–292.

56 N. S. Sanjini and S. Velmathi, CuO impregnated mesoporous silica KIT-6: a simple and efficient catalyst for benzene hydroxylation by C–H activation and styreneep oxidation reactions, *J. Porous Mater.*, 2016, **23**, 1527–1535.

57 B. Li and Y. Wang, Facile synthesis and photocatalytic activity of ZnO–CuO nanocomposite, *Superlattices Microstruct.*, 2010, **47**, 615–623.

58 R. Saravanan, S. Karthikeyan, V. K. Gupta, G. Sekaran, V. Narayanan and A. Stephen, Enhanced photocatalytic activity of ZnO/CuO nanocomposite for the degradation of textile dye on visible light illumination, *Mater. Sci. Eng. C*, 2013, **33**, 91–98.

59 S. Cen, W. Li, R. He, J. Tan, H. Wang, C. Wei and Y. Tang, Preparation of an ion imprinted functionalized mesoporous silica for rapid and specific absorption Cr (III) ions in effluents, *RSC Adv.*, 2017, **7**, 37778–37786.

60 P. V. Dong, C. H. Ha, L. T. Binh and J. Kasbohm, Chemical synthesis and antibacterial activity of novel-shaped silver nanoparticles, *Int. Nano Lett.*, 2012, **2**, 9.

61 Y. Li, W. Zhang, J. Niu and Y. Chen, Mechanism of photogenerated reactive oxygen species and correlation with the antibacterial properties of engineered metal-oxide nanoparticles, *ACS Nano*, 2012, **6**, 5164–5173.

62 K. M. Reddy, K. Feris, J. Bell, D. G. Wingett, C. Hanley and A. Punnoose, Selective toxicity of zinc oxide nanoparticles to prokaryotic and eukaryotic systems, *Appl. Phys. Lett.*, 2007, **90**, 213902.

63 Z. Emami-Karvani and P. Chehrazi, Antibacterial activity of ZnO nanoparticle on gram-positive and gram-negative bacteria, *IJP*, 2011, **5**, 1368–1373.
64 D. Paul and S. Neogi, Synthesis, characterization and a comparative antibacterial study of CuO, NiO and CuO–NiO mixed metal oxide, *Mater. Res. Express*, 2019, **6**, 055004.
65 J. R. Morones, J. L. Elechiguerra, A. Camacho, K. Holt, J. B. Kouri, J. T. Ramírez and M. J. Yacaman, The bactericidal effect of silver nanoparticles, *Nanotechnology*, 2005, **16**, 2346–2353.
66 K. R. Raghupathi, R. T. Koodali and A. C. Manna, Size–dependent bacterial growth inhibition and mechanism of antibacterial activity of zinc oxide nanoparticles, *Langmuir*, 2011, **27**, 4020–4028.
67 H. M. Yadav, J. S. Kim and S. H. Pawar, Developments in photocatalytic antibacterial activity of nano TiO_2: a review, *Korean J. Chem. Eng.*, 2016, **33**, 1989–1998.